

An Overview of the Results from an 8200 Hour Wear Test of the NSTAR Ion Thruster*

J. E. Polk, J.R. Anderson, J. R. Brophy, V. K. Rawlin, M. J. Patterson,
J. Sovey, J. Hamley

Abstract

A major component in validating ion propulsion for use on future deep space and earth orbital missions is demonstrating that the engines have sufficient service life capability. An 8200 hour test of a 30 cm engineering model thruster operating at 2.3 kW has been completed as part of a ground test program to support the development of the hardware for the Deep Space 1 technology validation mission. The primary objectives of the test were to identify any previously unrecognized failure modes, characterize the drivers of known failure modes and measure the performance degradation due to engine wear. A battery of diagnostic instruments were used to monitor engine wear and performance during the test, and a detailed post-test analysis of the engine was conducted. The performance degradation was minimal and the engine wear in general supports the conclusion that the technology has a very long service life capability. This paper provides an overview of the observed changes in performance and wear characteristics.

Introduction

Xenon ion propulsion is finally entering an age of application in NASA's planetary program. A xenon ion primary propulsion system is one of the key technologies being demonstrated on Deep Space 1, the

first of the New Millennium missions [1]. This spacecraft was launched in October, 1998 and will fly by an asteroid in 1999 and two comets in 2001. Ion propulsion was considered an enabling technology for the ST-4/Challengenger comet rendezvous mission [2], which is slated for launch in 2003. In addition, a number of Discovery mission proposals for small body rendezvous and Mercury orbiter missions have been submitted in the last three years. Solar electric propulsion is now considered a critical technology for proposed missions in the 2005-2010 time frame such as Europa Lander, Neptune Orbiter, Saturn Ring Explorer, Venus Sample Return and Comet Nucleus Sample Return.

NASA's 30 cm xenon ion thruster technology is being validated for use in near-Earth and planetary missions in the NASA Solar Electric Propulsion Technology Application Readiness (NSTAR) program. This program is designed to develop the industrial capability to produce flight engine, power processor and propellant feed system hardware and demonstrate that the technology is mature enough for flight applications. The technology validation portion of the program is focussed largely on providing flight program managers with sufficient information on performance, reliability and spacecraft interactions to allow them to use the technology.

The technology validation involves a large ground test program concentrating on the characterization of engine performance as a function of time and power level, specification of the engine and plume interactions with the spacecraft, and understanding the dominant engine failure modes. The program includes a number of long duration tests to identify unexpected failure modes, characterize the parameters which drive known failure mechanisms and determine

*Copyright 1999 by the American Institute of Aeronautics and Astronautics, Inc. The U.S. Government has a royalty-free license to exercise all rights under the copyright claimed herein for governmental purposes. All other rights are reserved by the copyright owner.

the effect of engine wear on performance. In the first test, 2000 hours of operation at the full power point, several potential failure mechanisms were identified and studied in subsequent shorter duration development tests. The effectiveness of design changes in essentially eliminating these failure modes was then validated in a 1000 hour wear test at the full power point, preparatory to starting an endurance test for the full 8000 hour design life. In this Life Demonstration Test (LDT), the most successful endurance test of a high power ion engine, a total of 8192 hours of operation were achieved at the 2.3 kW full power point before it was voluntarily terminated. A total of 88 kg of xenon propellant was processed, producing a total impulse of 2.73×10^6 Ns. In this paper the engine performance changes that occurred over the test will be described along with engine wear characteristics. The potential failure modes and wear processes are identified and the interaction of engine wear and performance degradation is discussed.

Description of the Engine, Facility and Test Conditions

The Wear Test Engine

The endurance test was conducted with the second Engineering Model Thruster (EMT2), fabricated by the Glenn Research Center (GRC)[3, 4]. The discharge chamber of the 30-cm. diameter engine has a conical upstream segment and a cylindrical downstream portion. The magnetic circuit is a ring-cusp design with samarium-cobalt magnet rings located near the discharge cathode in the rear of the chamber, at the transition between the conical and cylindrical segments and at the upstream end near the ion optics. The two-grid, molybdenum optics and the hollow cathode technology are derived from the 30-cm. mercury engine development program, although the cathodes incorporate improved heater materials and handling procedures developed for the Space Station Plasma Contactor Program.

The flight engines fabricated by Hughes Electron Dynamics (HED) incorporate several minor design changes which are not included in the EMT2 design. In the wear test engine the discharge chamber is fabricated from spun aluminum and titanium parts, while the flight design uses titanium for the entire discharge chamber. In addition, the gimbal bracket has been

changed from stainless steel to titanium and some of the discharge chamber components have lightening holes in the flight design. Grit-blasted wire mesh which covers the upstream, conical portion of the discharge chamber for improved sputter containment in EMT2 has been extended to cover the downstream portion as well in the flight design. Many of the components in the flight thruster are being grit blasted to improve thermal radiation capability compared to EMT2. The flight design also uses slightly stronger magnets which have been thermally stabilized at a higher temperature. In EMT2 the main cathode keeper assembly is attached to the discharge chamber, while the flight design uses a brazed cathode-keeper assembly. These design changes have been validated by analysis or test and are not expected to negatively impact engine performance or wear characteristics.

Vacuum Facility and Support Equipment

The test was conducted in a 3 m diameter, 10 m long stainless steel vacuum chamber pumped by three 1.22 m diameter CVI cryopumps with a pumping speed of about 45–50 kL/s on xenon and 3 xenon cryopumps consisting of 0.69 m² pure aluminum panels mounted on Cryomech AL200 coldheads with a pumping speed of about 18,000 L/s each, for a total speed of 100 kL/s. The development of the xenon cryopumps is discussed in more detail in [5]. This pumping system provides a no-load pressure of about $1\text{--}3 \times 10^{-5}$ Pa ($1\text{--}2 \times 10^{-7}$ Torr) and less than 5×10^{-4} Pa (4×10^{-6} Torr) at the full power flow rates. Approximately every 1000 hours these pumping surfaces had to be regenerated, which exposed the engine to an atmosphere composed primarily of xenon at a pressure of about 4000 Pa (30 Torr). The cathodes were purged during these exposures and reconditioned after subsequent pumpdown to high vacuum. These events were usually accompanied by a short term (about 6 hour) increase in the high voltage recycle rate and temporary increase in the neutralizer keeper voltage and coupling voltage, but otherwise appear to have no long term effects on engine operation.

To reduce the amount of facility material backsputtered onto the engine, the walls and rear of the chamber are lined with graphite panels. The backsputter deposition rate, monitored with a quartz crystal microbalance (QCM) mounted next to the engine in

the plane of the grids, was $0.16 \text{ mg/cm}^2\text{hr}$ or $0.7 \text{ } \mu\text{m/hr}$.

The propellant feed system used in the 1000 hour test [6] was modified for use in this test to include closed-loop flow control. This was accomplished by adding solenoid-driven micrometer valves in parallel with the manual micrometer valves used in the previous test. The manual valves provide a minimum purge flow during facility power outages and serve as a redundant flow control option in the event of a solenoid valve failure. All flow control valves were mounted inside the chamber, so that all external gas fittings had internal xenon pressures above atmospheric pressure to prevent leakage of air into the feed lines. The solenoid valves were driven by controllers with input signals from flow meters. This approach reduced the day-night fluctuations noted in the 1000 hour test [6]. The flow system was still subject to fluctuations of a few percent with a period of several minutes, which produced corresponding variations in the discharge voltage and current. Initial calibrations of the flow meters using three different calibration standards yielded results which agreed to within 1 percent. The flow meters were re-calibrated every 1000 hours and the flow meter zeroes were checked every 50-200 hours. Although the zero stability was excellent, the flow meter response did systematically drift over the course of the test. The main flow meter response for a given flow increased by about 3.5 percent, while the cathode flow meter responses decreased by 2 to 3 percent. This behavior is not unexpected in thermal mass flow meters and is most likely caused by changes in the thermal contact of the heater and RTD elements due to thermal cycling. The periodic recalibrations were sufficiently frequent to control the effect of this drift on the flow rate measurements.

The first 2974 hours of the wear test were conducted using a breadboard power processing unit (BBPPU) built by the Glenn Research Center which is described in detail in [7]. The test was continued using laboratory power supplies after the failure of the beam power supply in the BBPPU. These supplies are the same used in the 1000 hour test [6], although the accelerator grid power supply was modified to permit high voltage recycles with the discharge current reduced to 4 A rather than 2 A.

Diagnostics

A computer data acquisition and control system was used to monitor facility and engine conditions and control the power supplies. Data were sampled and stored to disk once every 4-5 seconds. The system was programmed to turn off the engine if out-of-tolerance conditions in certain facility or engine parameters were detected to allow unattended operation. This system recorded engine electrical parameters measured to within ± 0.5 percent with precision shunts and voltage dividers and mean flow rates measured to within ± 1 percent with the thermal mass flow meters.

The thrust was measured directly in the first 3100 hours of the test using a modified version of the GRC inverted pendulum thrust stand [8]. The thrust stand deflection, measured with a linear variable differential transducer (LVDT), was calibrated in-situ by applying small weights. Long-term drift in the thrust stand response was on the order of 1 percent. At each of the measurements, conducted every 50-200 hours, ten thrust stand calibrations were performed. Static friction in the thrust stand calibration mechanism contributes an uncertainty in the response of about $\pm 0.5 \text{ mN}$. Additional uncertainties in the measurement of the LVDT voltage yield a total uncertainty in the thrust measurement of about $\pm 1.1 \text{ mN}$. At 3100 hours a failure in the closed loop control of the thrust stand inclination left the thrust stand inoperable.

The ion beam characteristics were measured with near- and far-field probes. The near-field probes included a 0.8 cm diameter molybdenum disk used to monitor the beam current density and a tungsten wire loop emissive probe used to measure the beam potential distribution. These probes were mounted on an arm that could be swung through the beam at distance of about 2.5 cm downstream of the ion extraction system. The Faraday probe was biased -20 V with respect to facility ground to repel electrons. The emissive probe was heated to incandescence and the floating potential was measured to obtain an estimate of the beam potential. A probe consisting of an array of rods mounted at the end of the chamber was used primarily to monitor the behavior of the thrust vector. This probe and the measurement results are described in detail in [9].

The double-to-single ion current ratio was monitored periodically with an ExB probe mounted in the rear of the chamber. This ion velocity filter is described in more detail in references [6, 10]. The collimating slits on this probe permit ions emitted from a strip 3.1 cm wide extending across the entire face of the ion engine to be sampled, so the measured current ratio represents the integral of the current ratio distribution across the thruster. Charge exchange reactions in the beam also influence the ratio measurements, and the results reported here have been corrected for the attenuation of the two species by charge exchange reactions occurring between the source and the probe.

Measurements of the grid perveance limit and electron backstreaming limit taken every 50-200 hours were used to monitor changes in ion optics performance. The screen grid, which is normally connected electrically to the discharge cathode, was periodically biased 20 V negative of cathode potential to measure the ion current collected by it. From these measurements the screen grid transparency to ions was determined. The erosion pattern on the downstream surface of the accelerator grid was monitored with a laser profilometer mounted on a positioning system used to scan the laser sensor across the center portion of the grid and to move the apparatus out of the beam when the engine was on. This in situ erosion monitoring system is described in more detail with measurements from the first 6500 hours of operation in [11].

Test Conditions

The power supply setpoints (measured at the thruster) and flow rates for the nominal full power operating point are listed in Table (1) with the beginning of life values of the dependent electrical and calculated performance parameters. These conditions, which match those of the 1000 hour test, were maintained for most of the endurance test. Every 1000 hours engine operation was characterized over the full power range at the six throttle points listed in Table (1). These do not correspond exactly to the current NSTAR throttling profile, but are used as standard test conditions to allow comparisons with previous data. Periodically other off-nominal operating conditions are tested to guide development of the throttle

table or study particular phenomena, such as engine sensitivity to small variations in the controlled parameters [12].

Engine Performance During the Test

The engine performance parameters that are of interest to mission designers are thrust and propellant flow rate as a function of total engine power. The degradation in engine performance over time must also be considered in trajectory analysis and mission planning. The changes in these parameters as well as the composite performance parameters, specific impulse and efficiency, at the nominal and throttled conditions will be discussed in this section.

The thrust and power for the nominal full power operating point are plotted as a function of run time in Fig. (1). The calculated thrust is based on the measured beam current and voltage, a constant value of 0.98 for the beam divergence correction and a correction for multiply charged ions based on a curve fit to centerline double ion current measurements as a function of propellant utilization efficiency in a 30 cm, ring-cusp inert gas thruster[13]. The uncertainty in the calculated values is on the order of ± 2.1 percent. The agreement between the measured thrust and the calculated thrust is excellent over the first 3100 hours, before the thrust stand levelling mechanism failed. The beam current and beam voltage were maintained at the nominal values over most of the test. The measured and calculated thrust decreased slightly between 1000 and 2200 hours as the beam current dropped from 1.76 A to 1.75 A, however. This was due to a software discharge current limit in the BBPPU which prevented operation above 14 A. Over this time period this limit made it impossible to maintain the beam current setpoint. When the software was modified at 2200 hours to permit higher discharge currents the beam current and thrust returned to the previous values. In general, however, the thrust is quite constant over the first 3000 hours, varying by ± 1 mN about a mean of 92.7 mN. Although there are no direct thrust measurements after the first 3000 hours, it appears that the thrust has remained essentially unchanged. The beam current and net accelerating voltage were set at fixed values and the beam diagnostics discussed below and in reference [14] suggest that the double-to-single ion current ra-

<i>Controlled Parameters</i>	Nominal Test Point	Throttle Points					
		1	2	3	4	5	6
Beam Supply Voltage, V	1100	1100	1100	1100	1100	1100	650
Beam Current, A	1.76	1.76	1.59	1.26	1.01	0.66	0.54
Accelerator Voltage, V	-180	-180	-180	-180	-180	-150	-150
Neutralizer Keeper Current, A	1.5	1.5	1.5	1.5	1.5	1.5	1.5
Main Flow Rate, sccm	23.7	23.2	21.6	16.8	12.5	8.0	6.0
Cathode Flow Rate, sccm	3.7	3.0	2.5	2.1	2.1	2.1	2.1
Neutralizer Flow Rate, sccm	3.0	3.0	2.5	2.1	2.1	2.1	2.1
<i>Dependent Parameters</i>							
Beam Voltage, V	1088	1091	1092	1096	1091	1093	634
Accelerator Grid Current, mA	8.6	9.4	7.1	4.6	3.2	1.7	1.5
Discharge Voltage, V	25.1	26.0	26.0	25.5	26.0	27.1	27.9
Discharge Current, A	12.8	11.8	10.4	9.1	8.1	5.3	4.8
Neutralizer Keeper Voltage, V	14.3	14.2	14.7	15.7	17.1	19.4	21.2
Coupling Voltage, V	-13.4	-13.8	-14.2	-14.2	-14.2	-13.9	-13.6
Power, kW	2.32	2.27	2.05	1.66	1.35	0.90	0.51
<i>Performance</i>							
Thrust, mN	92.6	92.5	83.8	66.9	52.8	34.8	21.6
Specific Impulse, s	3170	3300	3290	3330	3300	2900	2200
Efficiency	.63	0.66	0.65	0.65	0.64	0.56	0.45
Discharge Loss, eV/ion	173	174	170	182	209	215	247
Propellant Efficiency	0.89	0.94	0.92	0.94	0.97	0.91	0.93

Table 1: Independent engine parameters and beginning-of-life dependent parameters and performance values

tio and the beam divergence remained constant. The behavior of the thrust vector over the course of the test is discussed in [9].

The power required to maintain this operating point increased over the course of the test from 2290 W to 2320 W. Most of this increase occurred over the first 3000 hours, and is due primarily to increases in discharge power, as discussed below.

Thrust measurements taken over the entire throttling range at the beginning of the test are shown with calculated beginning-of-life thrust in Fig. (2). The difference between the measured and calculated values is less than 1 mN. The calculated thrust was essentially constant as a function of time, because the engine operating conditions which enter the thrust calculation were controlled. The double ion content for the three lowest power levels increased with time, which could cause a decrease in thrust of up to 1 percent, when the ratios of double-to-single ion current integrated over a thruster diameter are cor-

rected to average ratios using the method discussed in [15]. The thrust vector probe indicated that the beam divergence did not changed dramatically. The true thrust is therefore likely to have remained near the calculated values. The power required to deliver that thrust increased with time over the whole throttle range, however, as the line of calculated thrust at 8192 hours in the figure demonstrates.

The propellant flow rates for the nominal operating point are shown in Fig. (3). The main and cathode flows were set to the nominal values for the entire test, except for a 100 hour period at about 3700 hours when a test at lower flows was conducted (referred to as the “100 Hour PAT Test” on subsequent figures). The neutralizer flow was constant until about 7000 hours, when it was raised to 3.6 sccm to match the value chosen for the NSTAR flight thruster. The main and cathode flows were the same for all of the throttling tests, but the neutralizer flow had to be increased at the lowest power levels to prevent plume

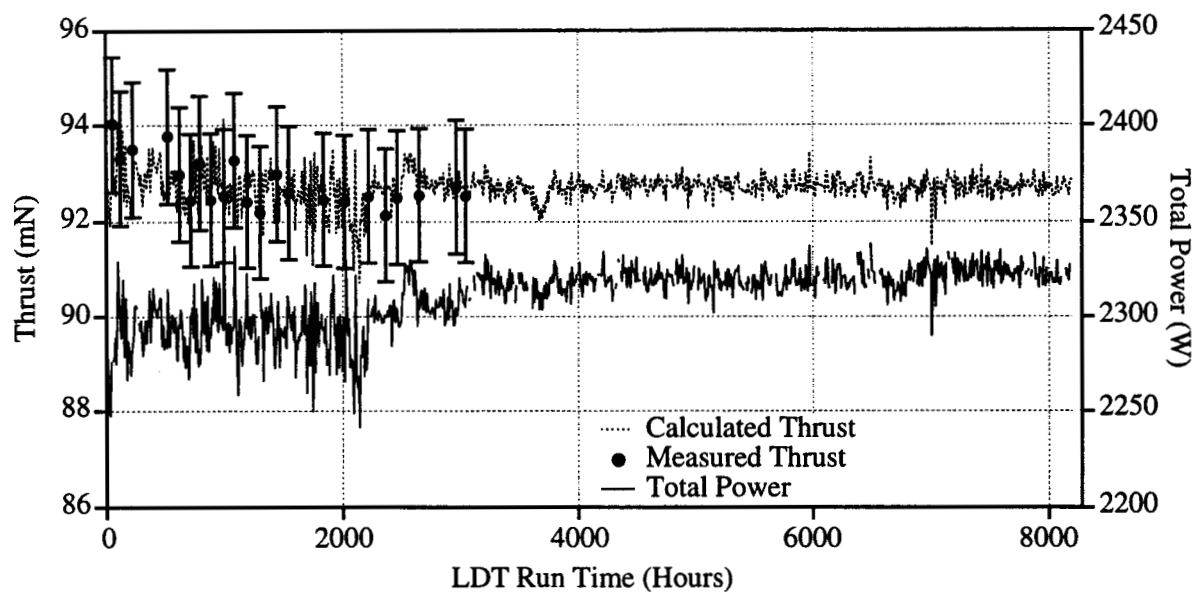


Figure 1: A comparison of measured and calculated thrust and total engine power requirements.

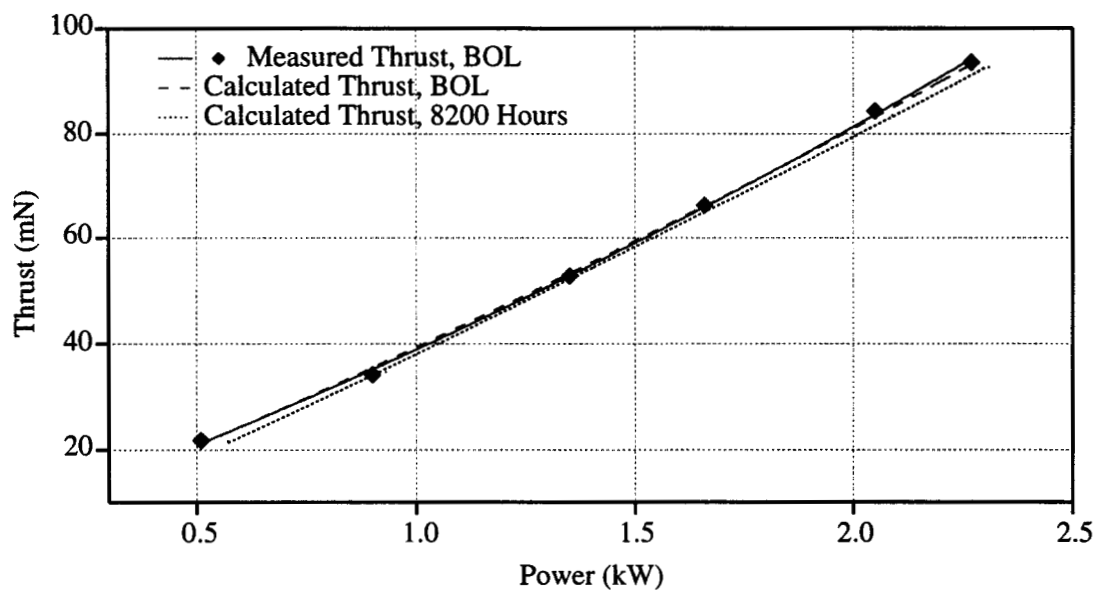


Figure 2: Comparison of measured and calculated thrust for the throttle test points.

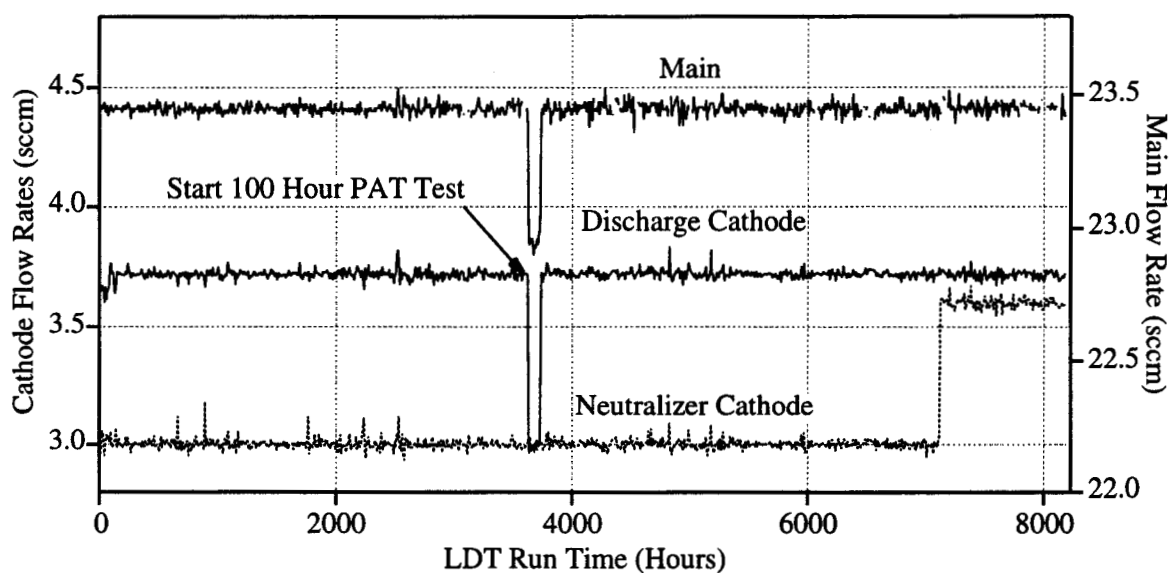


Figure 3: Flow rate history for the full power operating point.

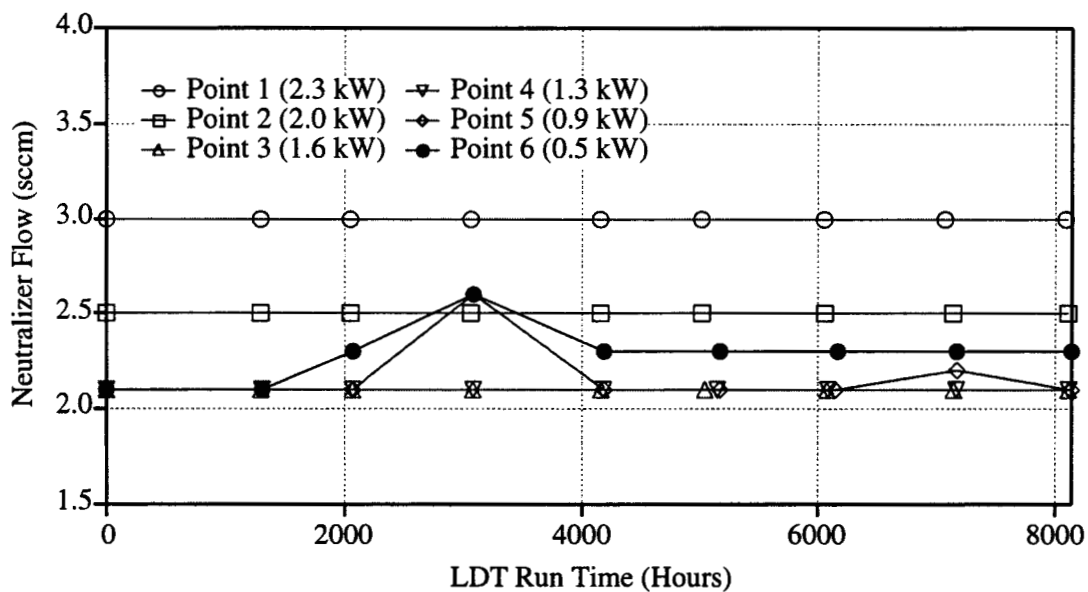


Figure 4: Neutralizer flow rates used in the throttling tests.

mode operation, as shown in Fig. (4).

The specific impulse and engine efficiency for the full power point are shown in Fig. (5). The Isp is essentially constant because the thrust and flow rates are controlled at fixed values. It drops only when the neutralizer flow is increased at 7000 hours. The efficiency drops at this point too, but also decays during the first 3000 hours due to the increasing engine power demands. The increase in power for a given thrust reduces the efficiency even more at the lower power operating points, as shown in Fig. (6). The efficiency losses are less than 1.5 percentage points for all but the lowest power level, at which a loss of 4 percentage points occurred. This is due in part to the higher neutralizer flows required at the lowest power, although this represents only about 0.9 percentage points of the total 4. As with the nominal full power test point, the efficiency decline is mainly due to increased discharge power requirements.

Analysis of Component Performance and Wear

Discharge Cathode Assembly

The performance of the cathode is defined by its ability to ignite reliably and supply electrons to the main discharge with a relatively low voltage. The performance of the cathode during the test will first be reviewed, then the results of post-test analysis of the cathode state will be presented.

Behavior During the Test. A total of 141 attempts to ignite the cathode were made during the LDT and in testing prior to the start of the wear test. The cathode failed to ignite after the first heat cycle on two occasions. The first was immediately after reconditioning the cathodes following a cryopump regeneration. In this case the cathodes were inadvertently conditioned initially at 8.5 A instead of the nominal 3.85 A normally used in the low heat phase. The discharge cathode lit successfully on the second heat cycle and performed normally thereafter. The second ignition failure occurred when the cathode was heated at 4 A instead of the nominal 8.5 A for part of the 210 s heating cycle. After an additional heating cycle at the correct heater current the discharge ignited properly.

The discharge current for the nominal operating point climbed from 13 A to 15.2 A as shown in

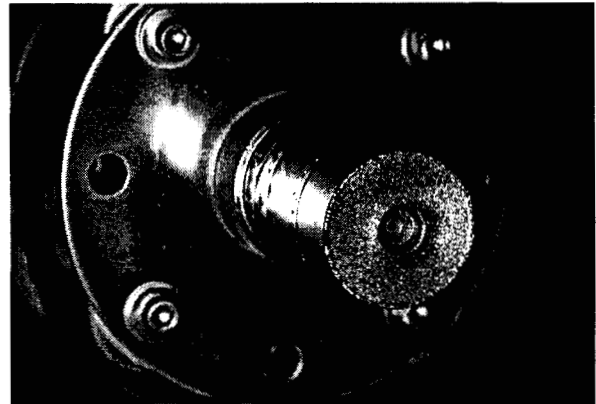


Figure 9: Photograph of the discharge cathode assembly in the discharge chamber.

Fig. (7). The discharge voltage dropped from 24.4 to 23.6 V, which is remarkably low for such an efficient thruster. These same general trends were observed at the throttled conditions as well. These data show no evidence of cathode performance degradation during the test. In this thruster the cathode keeper electrode is tied to the anode through a 1 kohm resistor, so it acts as an ignitor electrode and then draws about 20 mA during steady state operation. The potential of the keeper relative to the cathode is plotted with the discharge voltage in Fig. (8). The voltage is sensitive to the local plasma density, electron temperature and potential. It is always positive at the full power point, but decreases as the discharge voltage decreases. At the minimum power point the keeper voltage can actually be slightly negative with respect to the cathode, perhaps because of a higher electron temperature.

The cathode assembly component isolation was checked periodically throughout the test and showed little or no leakage current across the insulators.

Wear and Material Deposition Sites. The cathode is subject to ion bombardment from the discharge chamber plasma and has in some previous tests experienced severe erosion [16]. Post-test analysis focused on identifying the wear and deposition sites and the sources of energetic ions. An overall view of the cathode assembly is shown in Fig. (9). The discharge cathode was disassembled and the individ-

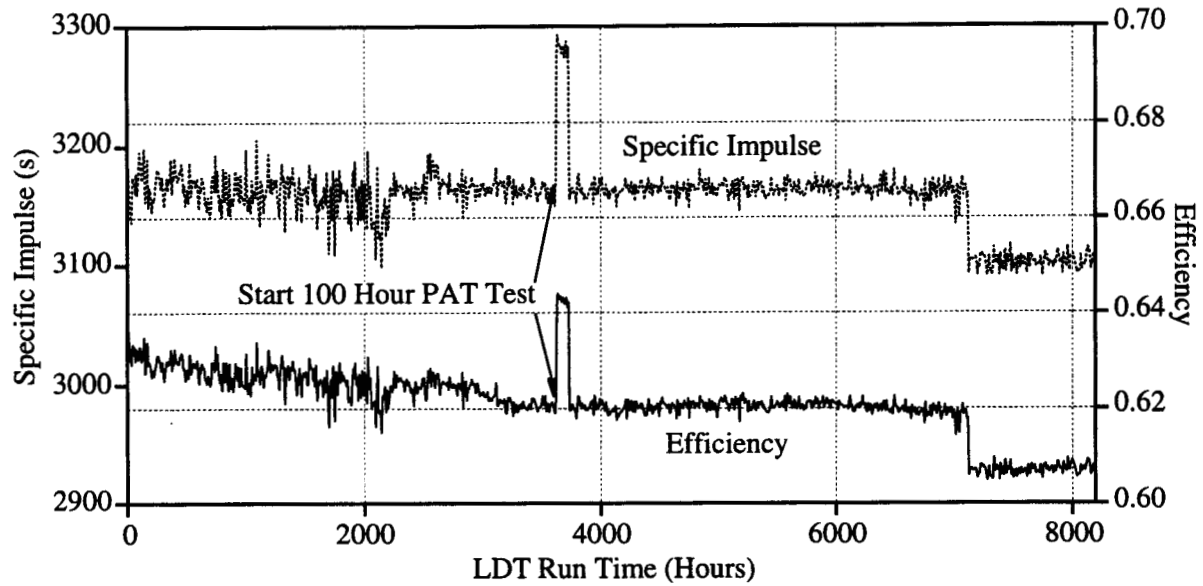


Figure 5: Specific impulse and efficiency for the nominal operating point.

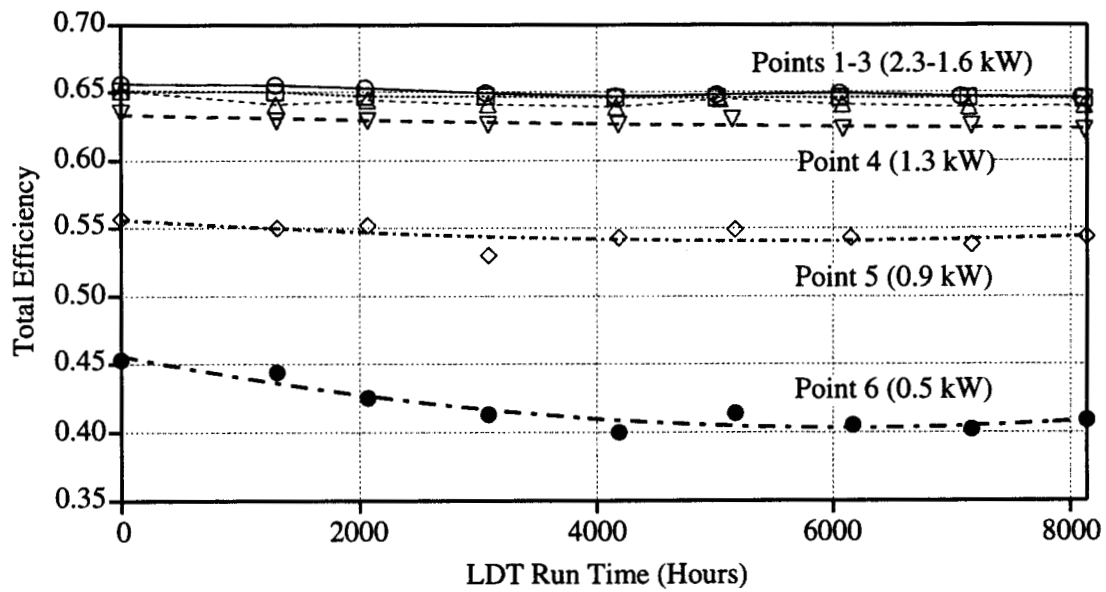


Figure 6: Efficiency as a function of time and power level for the throttle test points.

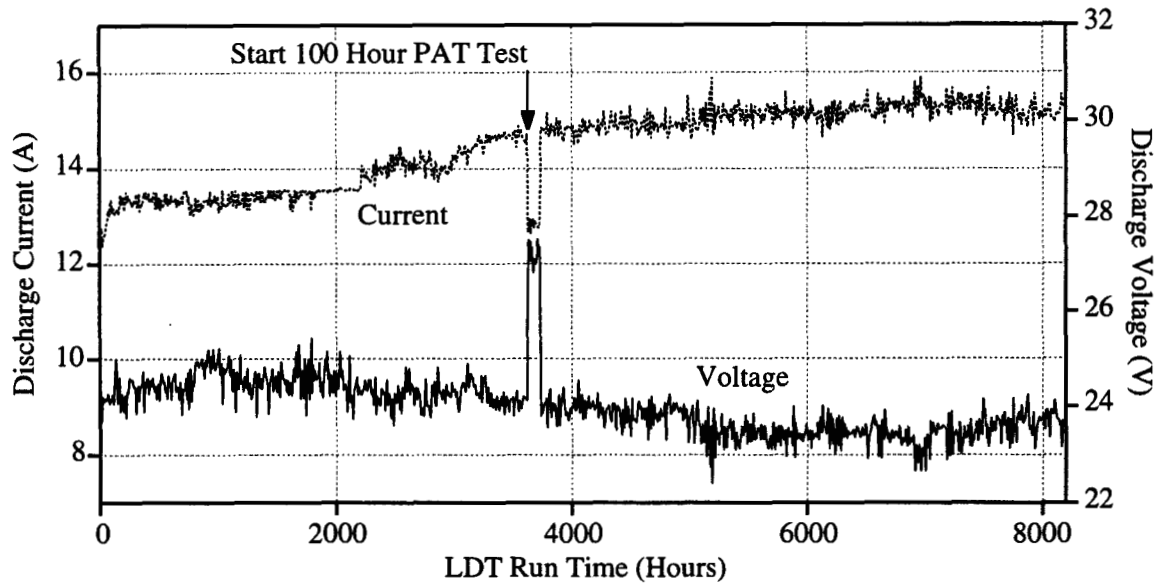


Figure 7: Discharge current and voltage for the nominal operating point.

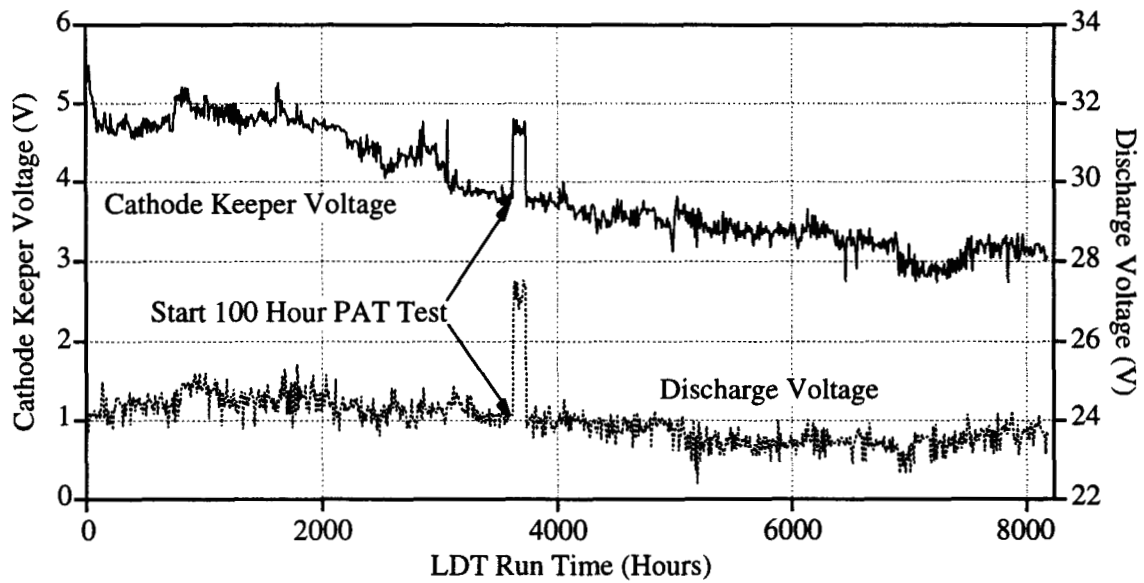


Figure 8: Variation of the discharge cathode keeper voltage and discharge voltage with time.

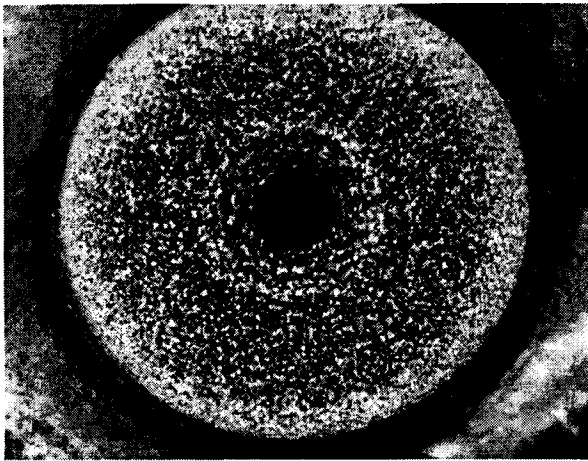


Figure 11: Photograph of the discharge cathode orifice plate after 8192 hours of operation.

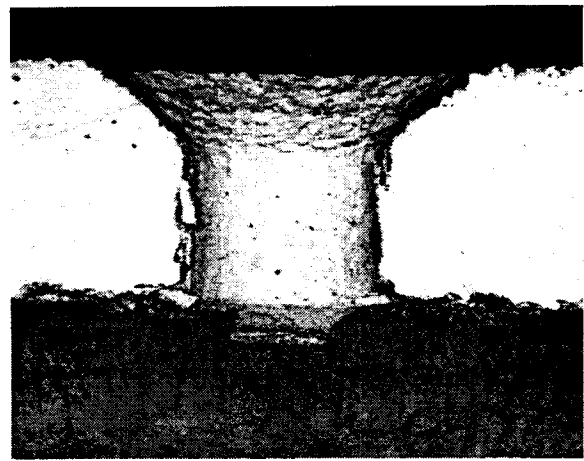


Figure 12: Cross-section of the discharge cathode orifice plate.

ual components were examined in a scanning electron microscope (SEM) using secondary electron and backscattered electron imaging and energy dispersive spectroscopy for composition analysis. The primary wear sites included the keeper orifice plate, the cathode orifice plate, and the downstream surface of the keeper flange.

The only significant erosion occurred on the downstream surface of the molybdenum keeper orifice plate. Figure (10) shows a cross section of one half of the orifice plate which was originally 1.52 mm thick. The maximum eroded depth was 32 to 36 percent of the total thickness on the two sections examined. In addition, the downstream end of the orifice has been significantly chamfered. The original 4.75 mm diameter has increased by 18 percent to 5.59 mm. The upstream diameter is 4.65 mm, slightly less than the pre-test value. The upstream face and the upstream half of the orifice are sites of net deposition, as can be seen in the cross section. The upstream deposits are up to 50 μm thick at the upstream edge of the orifice and are composed primarily of tungsten. Traces of barium, calcium and molybdenum were also found on the upstream face. The keeper orifice plate-to-keeper tube weld was eroded slightly on the downstream side, but was still structurally sound.

The downstream face of the cathode orifice plate has been textured by sputter erosion as shown in Fig. (11) The inner, darker zone is slightly more heav-

ily textured and has a diameter of 4.78 mm, almost exactly the same as the keeper orifice diameter. A cross section of the cathode orifice plate is shown in Fig. (12). The downstream surface texturing has not appreciably changed the plate thickness. The downstream diameter of the orifice chamfer is also the same as the pre-test specification. The orifice diameter is 0.94 to 0.96 mm, which is slightly less than the pre-test value of 1.00. The upstream face appears to have some eroded areas near the entrance to the orifice, but there is also evidence of net deposition, which was also noted after a long duration test of a plasma contactor cathode [17]. The upstream face of the orifice plate is covered with fine tungsten crystals which form a solid film at the entrance to and inside the orifice. Barium was also detected on this surface. The weld on the side of the cathode orifice plate shows no signs of damage. Overall, the erosion of the cathode orifice plate is minimal.

The downstream face of the stainless steel keeper flange which is welded to the tantalum keeper tube has a shiny inner ring and a matte finish on the outer periphery. SEM exams of the inner ring reveal tantalum deposition and a sparse collection of sputter cones on eroded stainless steel. The outer ring has a much denser collection of sputter cones, which is what produces a dull finish. Many of the cones have tantalum and molybdenum deposits on the tips. The damage to this component is negligible.

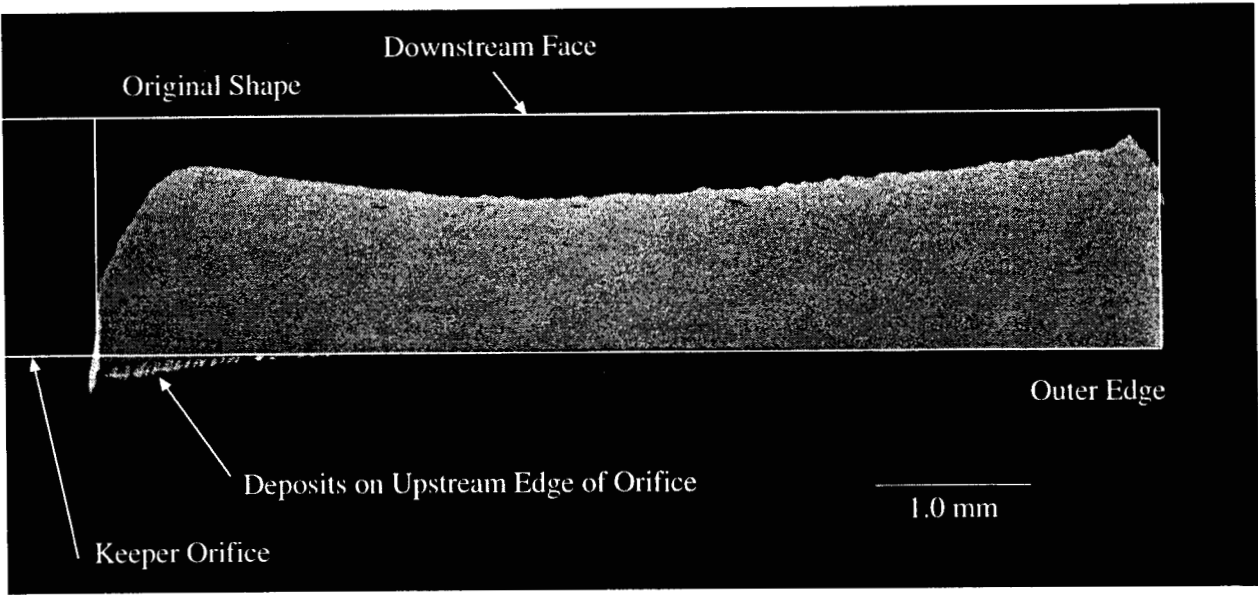


Figure 10: Cross-section of the discharge cathode keeper orifice plate.

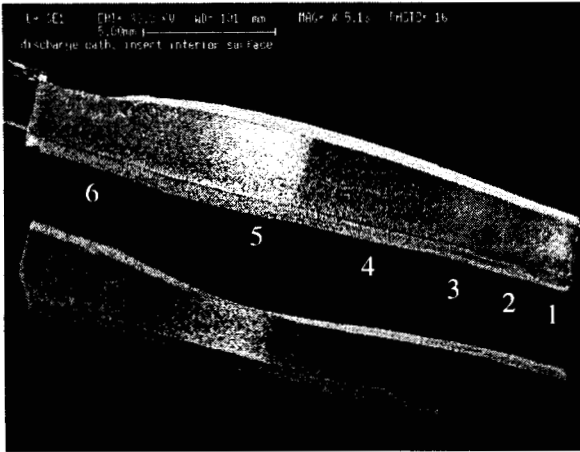


Figure 13: Six zones on the interior of the discharge cathode insert.

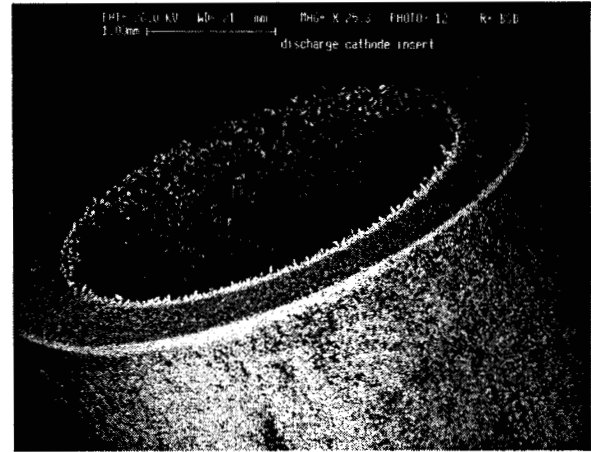


Figure 14: Photograph of the discharge cathode insert showing crystals forming near downstream end.

Insert Characterization. The cathode insert was removed and fractured in order to characterize the emitter surface. Six distinct zones found along the axis of the insert are identified in Fig. (13). A region about 2 mm long at the downstream end of the insert tube was densely covered with fine tungsten crys-

tals and a less dense covering of much larger crystals, as shown in the photomicrograph in Fig. (14). This coating did not appear to completely cover the virgin surface of the impregnated insert and regions with barium deposits were found in this zone. A 2 mm re-

gion upstream of the first zone was also covered with the small crystals and some large ones, but had very little barium on the surface. A third region about 1.7 mm long upstream of that had a surface similar to a new sintered insert with some of the smaller crystals. This region also had some barium deposits in the matrix. A region about 5.3 mm long in the center of the insert tube was composed of a sintered porous tungsten matrix with very little evidence of barium. The surface of a fifth region about 3.7 mm long near the upstream end of the insert was almost completely covered with a coating containing barium, calcium, aluminum and oxygen—presumably the original impregnate material. The upstream end of the tube was primarily the tungsten matrix with isolated patches of barium, calcium, aluminum and oxygen in the pores.

The fracture surfaces were also examined and a reduced barium content was found in layers ranging from 45 to 135 μm thick on both the inner and outer surfaces of the insert tube. A substantial amount of the impregnate was found on the inner surfaces of the cathode tube which had been in contact with the insert. Apparently the impregnate diffuses out of any free surface during operation. Deposits of the impregnate material were also found in the upstream end of the cathode tube where it is joined to the insulator. This area is probably considerably cooler than the downstream regions, so material evaporated from the insert tends to condense there.

Condition of Joints and Insulators. As mentioned above, the structural integrity of the weld joints was not threatened in this test. The metal-to-insulator braze joints did not appear to be as sound, but a detailed analysis was not performed because the braze process was improved after the fabrication of this thruster. The primary insulator between the cathode tube and the anode had a metallic deposit on the downstream surface that may have come from material in the braze joints. The insulator design incorporated a groove for shadow-shielding, which successfully prevented shorting.

Neutralizer Cathode

The neutralizer cathode performance is evaluated in terms of its ignition reliability and ability to efficiently supply electrons to neutralize the beam. The

neutralizer was subjected to the same kind of analyses as the discharge cathode after the test.

Behavior During the Test. A total of 139 neutralizer ignitions occurred prior to and during the test. The neutralizer never failed to ignite on the first attempt with the 650 V ignitor pulses from the BBPPU or with the 40 VOC capability of the laboratory supply used for the last part of the test.

The neutralizer keeper voltage and the magnitude of the coupling voltage (which was always negative with respect to facility ground) for the nominal operating point with a keeper current of 2.0 A are shown in Fig. (15). These voltages show the same basic behavior. Although there are transient increases associated with the exposure to residual gases during pump regenerations and subsequent reconditioning, the overall trend is decreasing. This is indicative of improving emitter surface conditions. Similar behavior was seen at the throttled conditions as well.

The neutralizer operation as a function of flow rate was characterized periodically over the entire throttling range to monitor changes in the flow rate margin. A certain minimum flow rate and total emission current are required to prevent plume mode operation, which is characterized by somewhat higher keeper voltages and much higher amplitude keeper voltage oscillations. Plume mode operation under certain conditions can greatly increase neutralizer wear rates. The flow rate boundary between stable spot mode operation and plume mode for the neutralizer operating in diode mode with no beam current is shown in Fig. (16). These data show that the transition flow rate increased with time, with the largest increase occurring in the first 1450 hours. Similar magnitude changes occurred at the other throttle points as well, although no single event during this time period could be identified that might have caused this deterioration. The transition flow rates measured at the end of the test are plotted as a function of beam current in Fig. (17). The current NSTAR throttling table is also plotted to show the flow rate margin.

Periodic measurements of the neutralizer assembly isolation showed increasing leakage current from the neutralizer keeper to the plasma screen. The final impedance was about 130 kohms, which was sufficient for proper neutralizer operation. Post-test examination showed that the leakage current was through thin films of carbon back-sputtered from the beam target

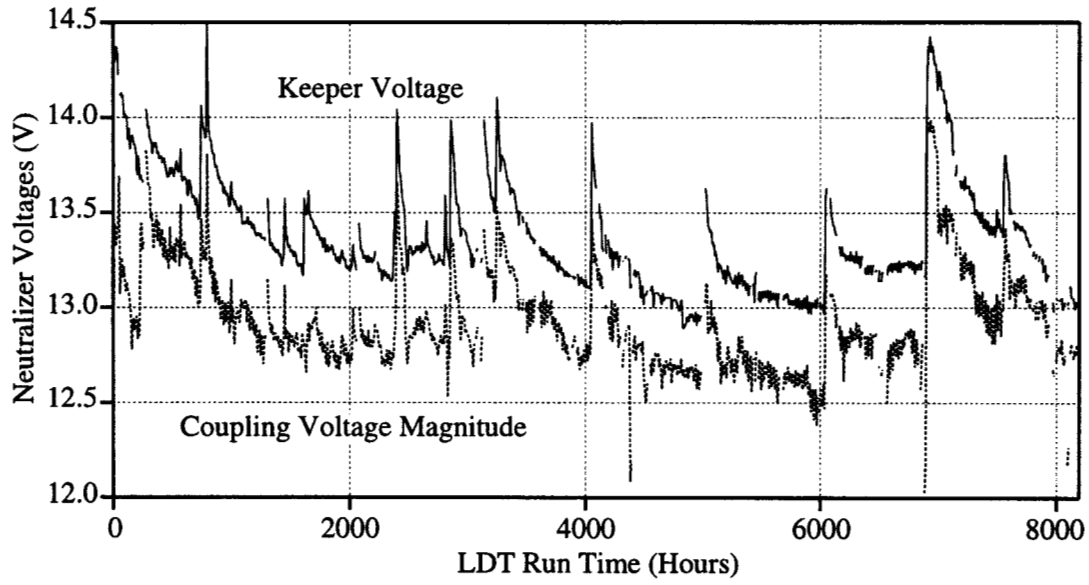


Figure 15: Variation of the neutralizer keeper and coupling voltages with time.

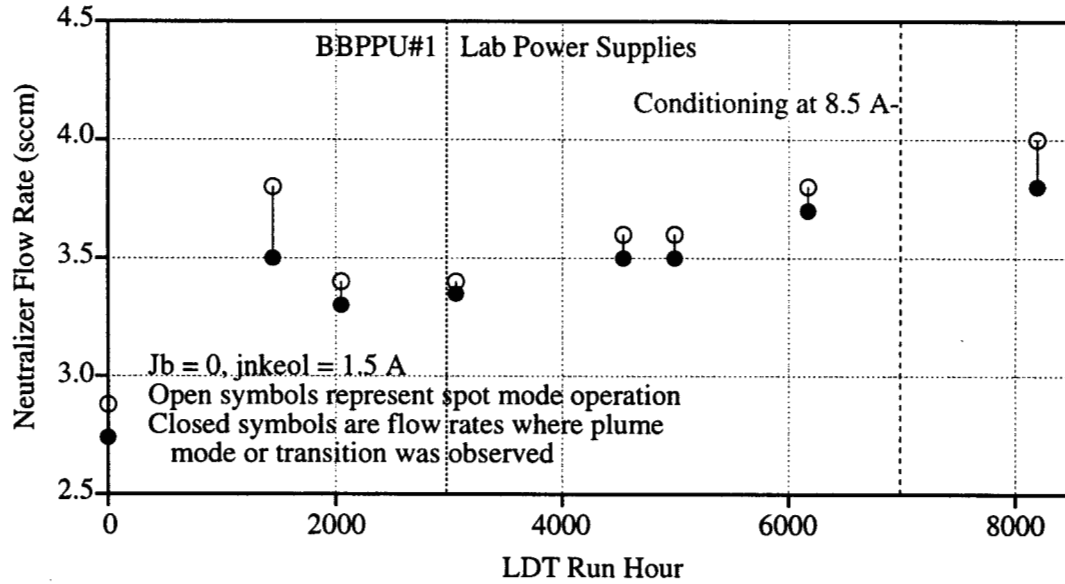


Figure 16: Flow rates required to maintain spot mode operation with no beam current.

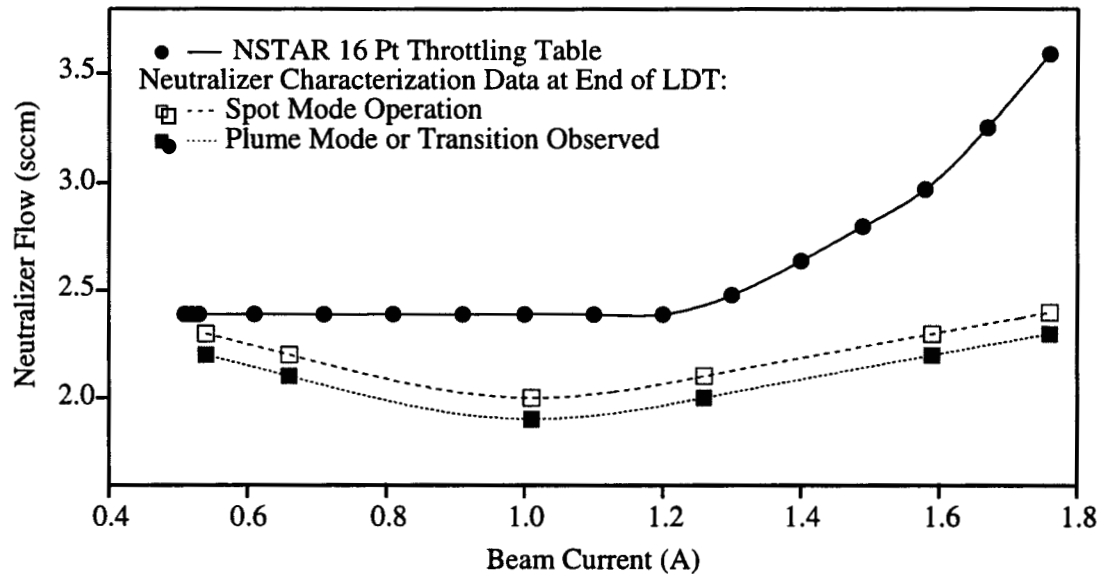


Figure 17: Margin between the NSTAR neutralizer flow rates and the transition from spot to plume mode.

onto some fiberglass sleeving used on the neutralizer wiring.

Wear and Material Deposition Sites. The neutralizer cathode was also disassembled and examined for signs of wear and material transport. The only significant wear site was the neutralizer cathode orifice, shown in cross section in Fig. (18). The upstream orifice diameter is essentially unchanged from the pretest value of 0.280 mm, while the downstream end of the orifice has increased by 70 percent to 0.48 mm. The surface of the chamfer is heavily textured from ion bombardment, but no significant dimensional changes have occurred. Small tungsten deposits up to about 10 μm in diameter were found inside the orifice near the upstream entrance. The upstream face of the orifice plate showed no signs of erosion, although a ring of barium deposits was found around the orifice. There was only slight surface texturing on the downstream face of the cathode orifice plate and no damage to the weld between the plate and the cathode tube.

The neutralizer keeper electrode also experienced very little wear. The downstream face and weld show no evidence of sputter damage. The upstream face of

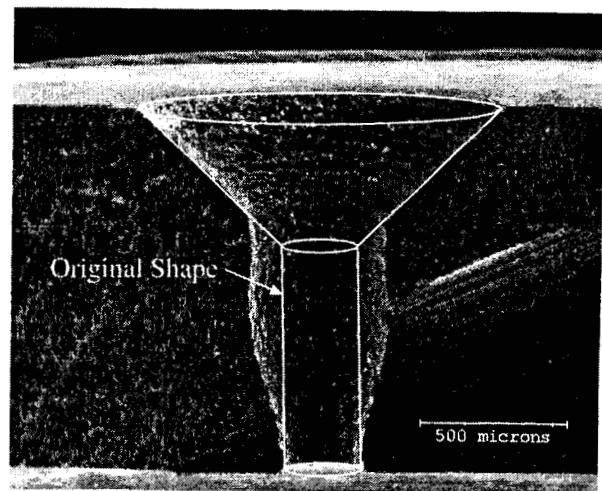


Figure 18: Cross-section of the neutralizer cathode orifice plate.

the molybdenum keeper has a thin deposit of tungsten around the orifice which must have come from the neutralizer orifice. A portion of the tantalum keeper tube was exposed to high angle beam ions and shows some surface texturing, but no significant mass loss.

Insert Characterization. The neutralizer insert was fractured to examine the interior emitting surface where distinct zones were also found. In this case they were distinguished primarily by the composition, not the microstructure. The entire interior surface still consists mostly of the original sintered tungsten matrix. The only tungsten deposits were found in a zone near the upstream end and they consisted of tiny crystals on the order of a μm in diameter on the sintered tungsten particles. The surface of a region about 1 mm long at the downstream end of the insert tube consisted of the tungsten matrix with very little barium. A second region 5.5–6.5 mm long upstream of that consisted of the matrix with isolated patches 10–30 μm in diameter that contained primarily barium. In the center section of the cathode insert the surface was mostly porous tungsten with little evidence of barium containing compounds. The upstream end of this region is where the tiny crystals were found. The matrix at the upstream end of the insert contained large amounts of material consisting of barium, calcium and oxygen, although the region where the insert was brazed to a molybdenum ring at the end contained less barium compounds.

Condition of Joints and Insulators. No deterioration was found on any of the welds or brazes or on the insulators in the neutralizer assembly.

Ion Optics

A number of ion optics performance parameters were measured periodically during the test at the nominal and throttled operating points. After the test the grids were examined for signs of wear, including sectioning and detailed SEM measurements of erosion site geometry.

Behavior During the Test. The beam current density and potential distributions measured about 2.5 cm downstream of the exit plane are shown in figures (19) and (20). The beam current density distribution is strongly peaked on the centerline and drops sharply 1–2 cm in radially from the periphery of the

hole pattern. These profiles did not change significantly over the test and yield average flatness parameters ranging from 0.32 at the minimum power point to 0.46 at full power. The peak beam potential ranges from 3.2 to 4.9 V, and is largest for intermediate power levels. Both distributions show peak offsets from the thruster centerline. This phenomena was quite repeatable and evidently represents a true deviation from axisymmetry in the beam.

Accelerator grid impingement current as a function of operating time for the nominal point and the six throttle points is displayed in Fig. (21). After an initial transient lasting about 1500 hours, the current was stable for all power levels. Transients in the detailed data for the nominal point include one period of operation at a higher tank pressure starting about 700 hours and episodes where carbon flakes spalling from the accelerator grid temporarily shorted it to the plasma screen, which was floating.

The perveance limit continuously decreased for all operating points, as shown in Fig. (22). This behavior in itself is not threatening because it increases the voltage margin over time. The electron backstreaming limit also varied continuously over the course of the test, as Fig. (23) shows. In this case the margin decreases with time. The margin at the end of the test is shown in Fig. (24), which displays the electron backstreaming limit data from the end of the test and the accelerator grid operating voltages. The screen grid transparency showed a similar monotonic change with time. The measurements plotted in Fig. (25) show about a 2–2.5 percentage point decline in the transparency at the high power and minimum power points and somewhat smaller changes at intermediate power levels. The high voltage recycle rate varied from about 1–2 per hour in this test. This is similar to other ground tests, although recent data from the DS1 flight show a recycle rate in space that is much lower [1]. The higher ground recycle rate may be due to higher pressures in the vacuum facility or the presence of contaminants back-sputtered from the beam target.

Wear and Material Deposition on the Accelerator Grid.

The total mass loss of the accelerator grid in this test was 10.81 g. Post-test measurements showed that the grid thickness had not changed significantly. The wear was distributed between two main sites: the

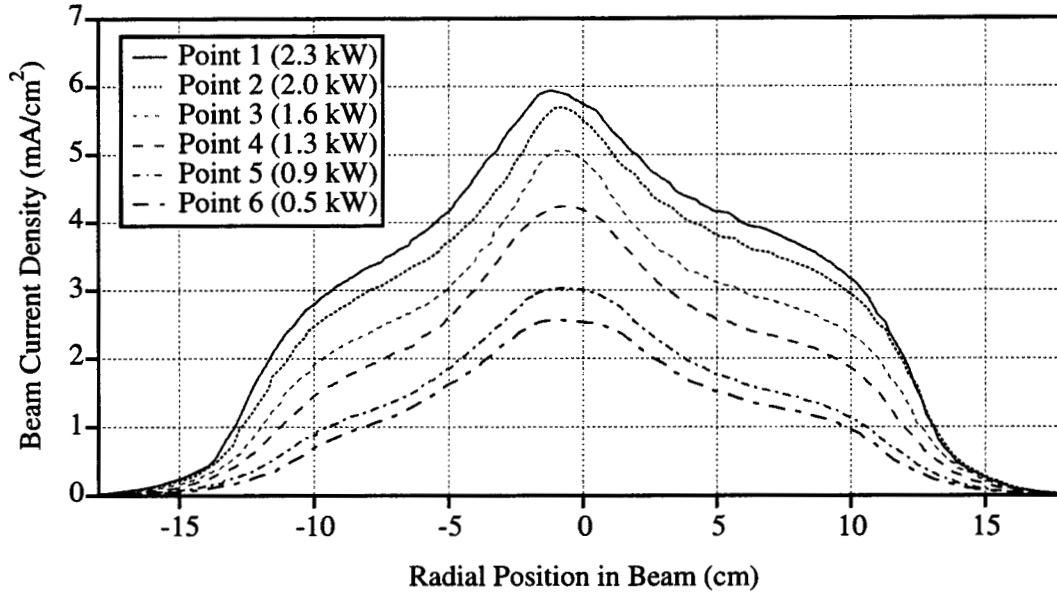


Figure 19: Beam current density distribution for the six throttle points.

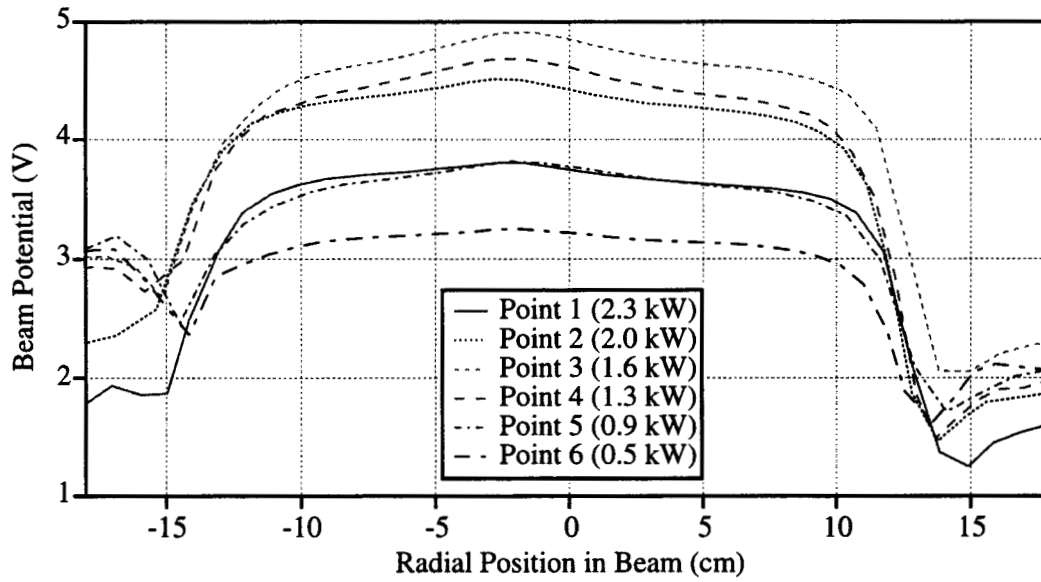


Figure 20: Beam potential measurements for the throttle test points.

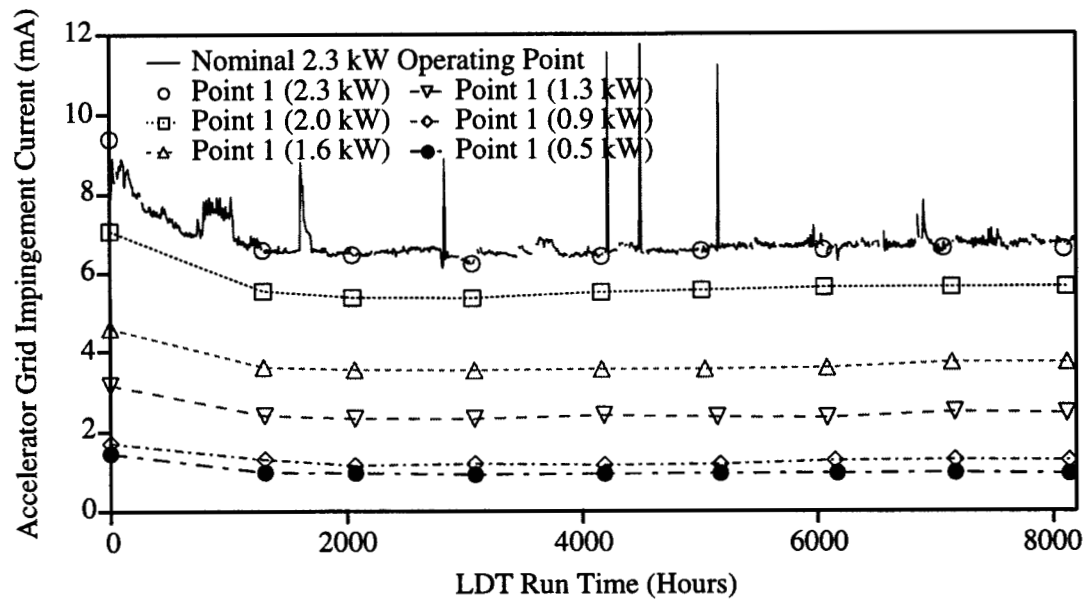


Figure 21: Accelerator grid impingement current time history for the nominal and throttle test points.

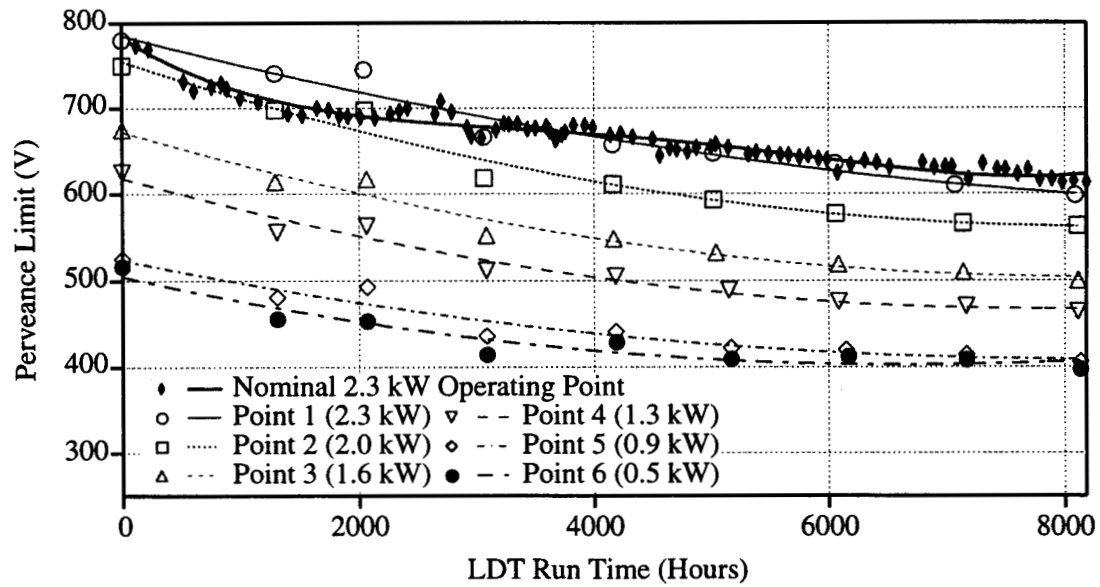


Figure 22: Perveance limit for the nominal and throttle test points.

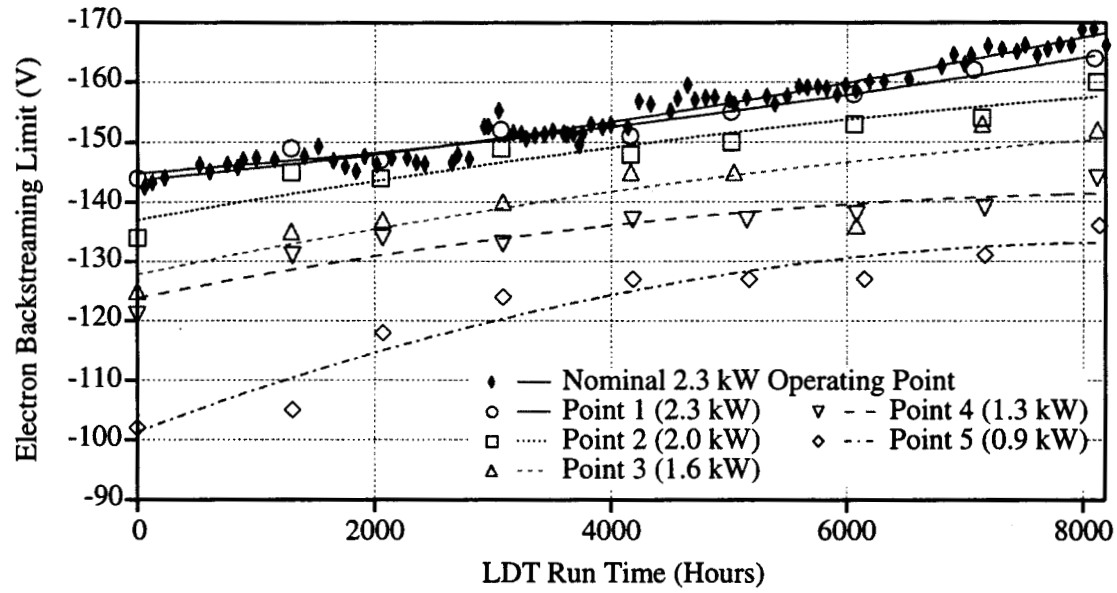


Figure 23: Electron backstreaming limit for the nominal and throttle test points.

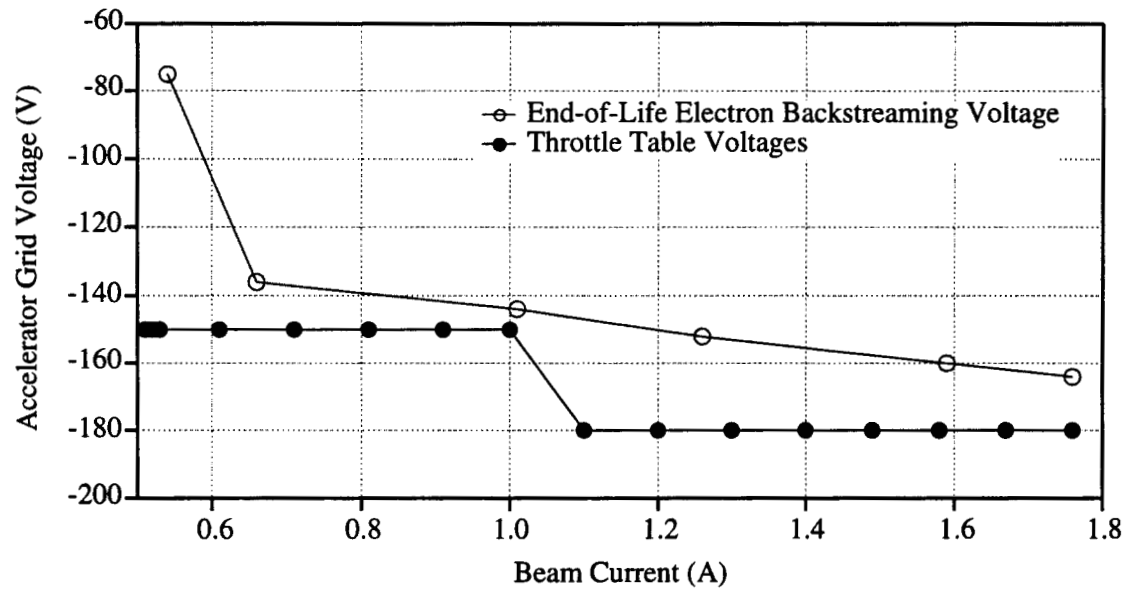


Figure 24: Electron backstreaming voltage margin at the end of the test.

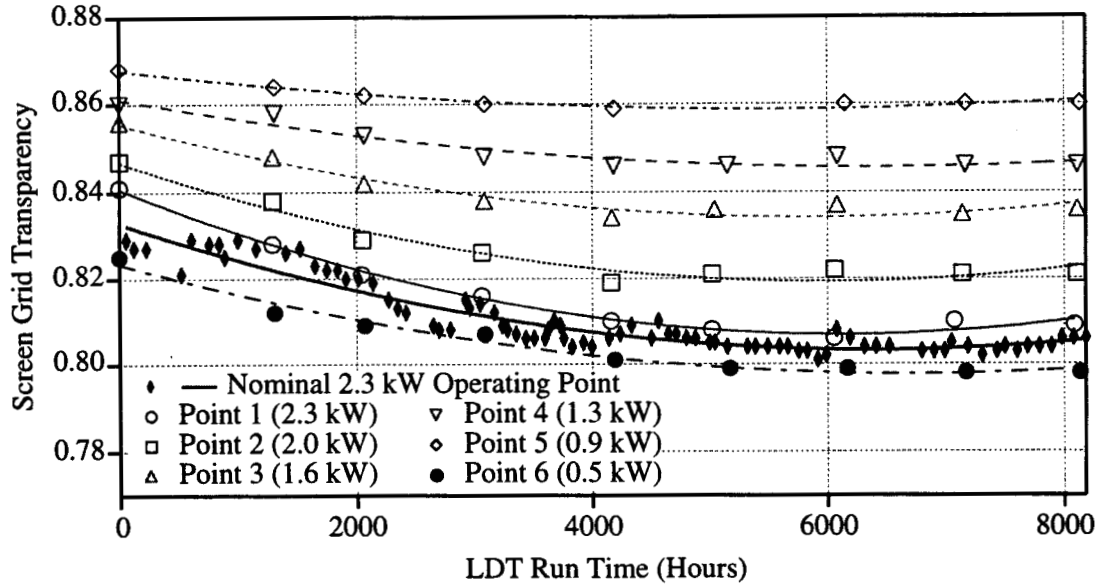


Figure 25: Screen grid transparency for the nominal and throttle test points.

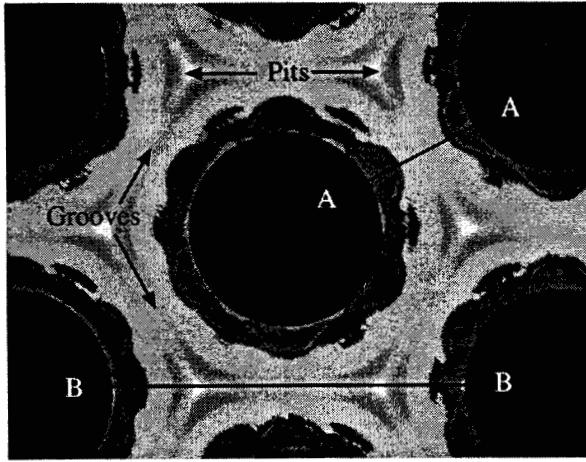


Figure 26: Major erosion and deposition sites on the accelerator grid.

walls of the apertures and the “pits and grooves” pattern on the downstream face. The image in Fig. (26) shows the pits and grooves pattern and a region of net carbon deposition around each aperture. The carbon is back-sputtered from the beam target onto

the engine, although the impingement current density is evidently sufficiently high in pits and grooves to prevent net deposition. This figure also shows two measurement paths. Path A-A and B-B were used as scan paths for the laser profilometer to characterize the erosion pattern in situ over the course of the test. After the test the grid was sectioned into small grid bits, which were then polished along these cuts to produce cross-sections of the erosion pattern that could be measured in an SEM. Figure (27) shows one of these cross-sections through B-B near the center hole. A cut along a diameter of one of the apertures shown in Fig. (28) clearly reveals the extent of aperture wall erosion near the center of the grid. In this case the cusps that normally extend into the aperture formed in the 50:50 photoetch process have been completely removed.

Time-resolved data from the profilometer were presented in reference [11]; in this paper the final set of profilometer data taken at the end of the test will be compared with the SEM measurements. The pit depth as a function of radius is plotted in Fig. (29). The two measurement techniques are in excellent agreement and show that the pit depth peaks off-axis

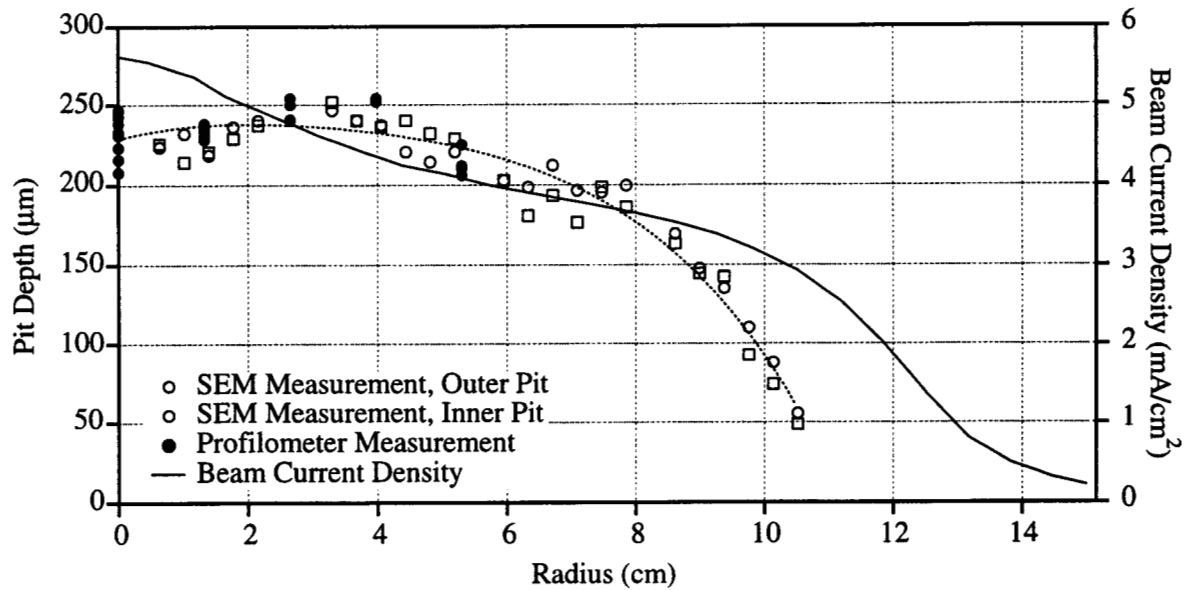


Figure 29: Pit depth as a function of radius on the accelerator grid.

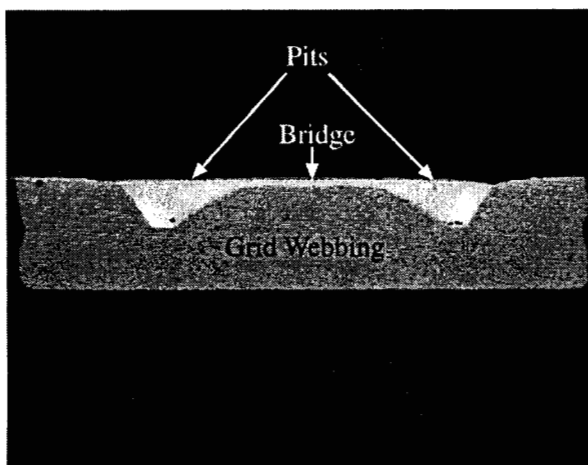


Figure 27: Cross-section of the accelerator grid showing the pits and grooves erosion pattern.

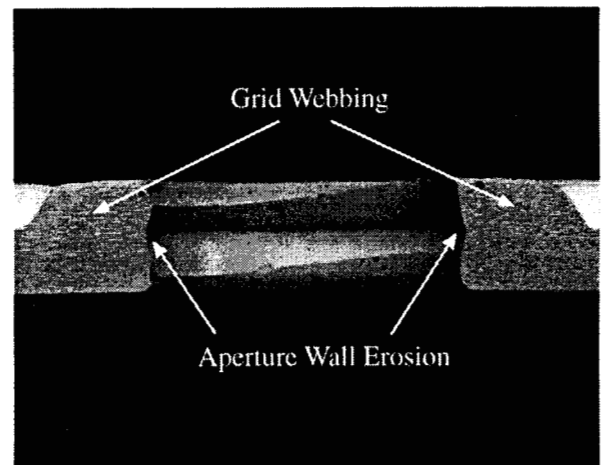


Figure 28: Cross-section of the accelerator grid showing erosion on the aperture wall.

at about 4 cm. Comparison with the beam current density profile reveals that the pit erosion magnitude drops more rapidly radially than the current density. The time-resolved profilometer measurements proved that the pit erosion rate is constant over time.

The bridge depth, or minimum groove depth, plotted in Fig. (30) shows excellent agreement between the SEM and profilometer measurements. The bridge depth also peaks off-axis and drops at about the same radial position as the beam current density. The profilometer data in [11] also showed a constant bridge erosion rate. The groove width measurements from the SEM agree well with the last set of profilometer measurements and suggest that the width is constant with radius, as shown in Fig. (31). However, weighted mean values of the profilometer data over the course of the test suggest that the groove width increases with radius as seen in previous tests [18]. The definition of the groove width in both measurements is somewhat arbitrary, so the differences may be within the uncertainty. These data indicate that the fraction of the webbing surface subject to erosion in the pits and grooves pattern is 0.41 in good agreement with previous measurements on NSTAR thrusters [6].

The volume of the pits and grooves was estimated from the profilometer and SEM data to obtain an estimate of the mass loss in these sites. This calculation yielded a value of 4.7 g, or about 43 percent of the total measured mass loss.

The aperture diameters were measured using precision ground pins with 0.013 mm accuracy and on the cross-sections with the SEM to within about 2 percent. These measurements are compared in Fig. (32). The agreement is good over most of the grid radius except from about 5 to 7 cm and 12 to 12.5 cm, where the measurements diverge. The pin measurements were used to estimate the overall open area fraction of the grid at the end of the test. It apparently increased from a pre-test value of 0.24 to 0.28, a 17 percent change in 8200 hours. These data were also used to estimate the total mass loss on the hole walls using a model for the geometry of mass removal which is discussed in [2]. The calculation yielded a value of 5.2 g. The sum of the estimated mass loss in the holes and on the downstream surface is 9.9 g, which agrees with the measured mass loss to within about 10 percent. These estimates suggest that the mass loss is split about equally between these two erosion

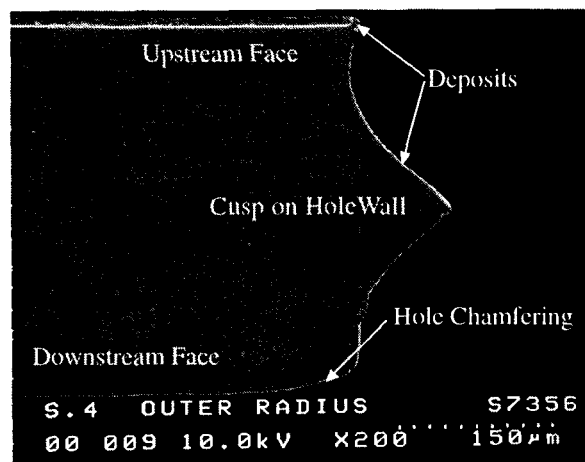


Figure 33: Cross-section of the screen grid showing regions of erosion and net deposition.

sites.

Wear and Material Deposition on the Screen Grid. The screen grid gained 0.73 g over the course of the test. The screen grid was also sectioned, and SEM examinations revealed a slight chamfering of the upstream inlet to the apertures in the grid center and sites of net deposition on the downstream surface, as shown in Fig. (33). The maximum depth the chamfer penetrates into the webbing and the width of the chamfer ring around the hole are plotted in Fig. (34). These data were used to estimate a total mass loss of about 0.23 g in this erosion site. Some of the screen grid bits were potted and carefully polished to obtain good images of the deposits. Thicknesses measured from these photomicrographs are plotted in Fig. (35). The deposits at the cusp reduce the diameter of the screen grid apertures by up to 2 percent, as shown in Fig. (36). Composition analysis in the SEM revealed that these deposits are molybdenum eroded from the accelerator grid apertures. These data were used to calculate a total of about 1.6 g of material deposited on the screen grid surfaces, yielding a net mass gain estimate of 1.37 g. This suggests that up to 31 percent of the mass removed from the accelerator grid apertures is deposited on the screen grid, which seems unreasonably high. The estimated net mass gain is about two times higher than the measured value, so the discrepancy is mostly likely due to an overestimate of the deposited mass.

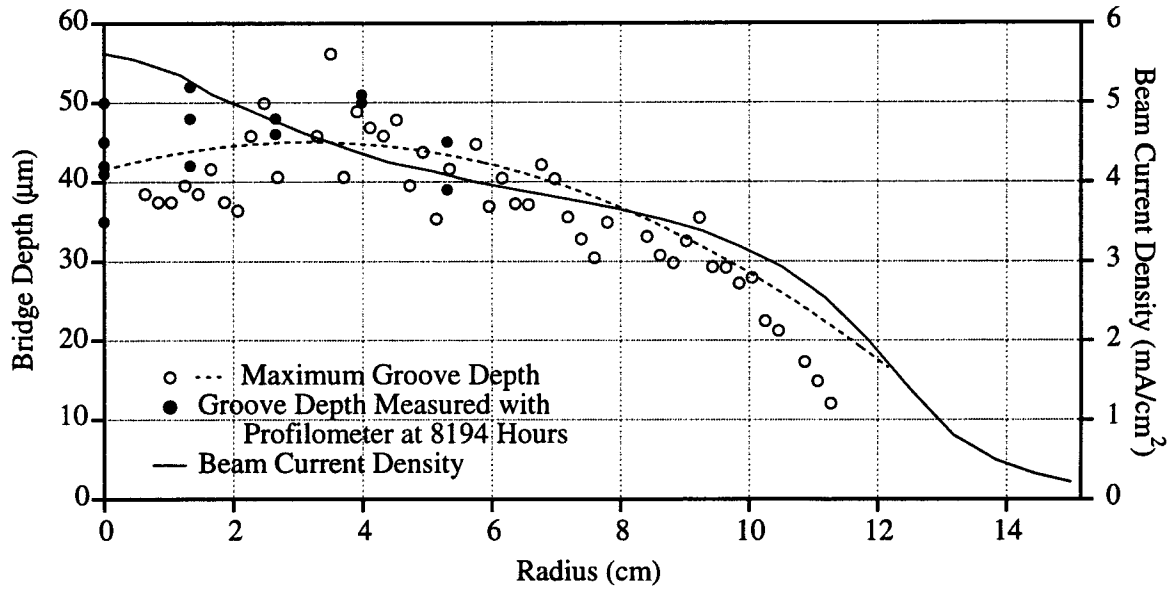


Figure 30: Bridge depths as a function of radius on the accelerator grid.

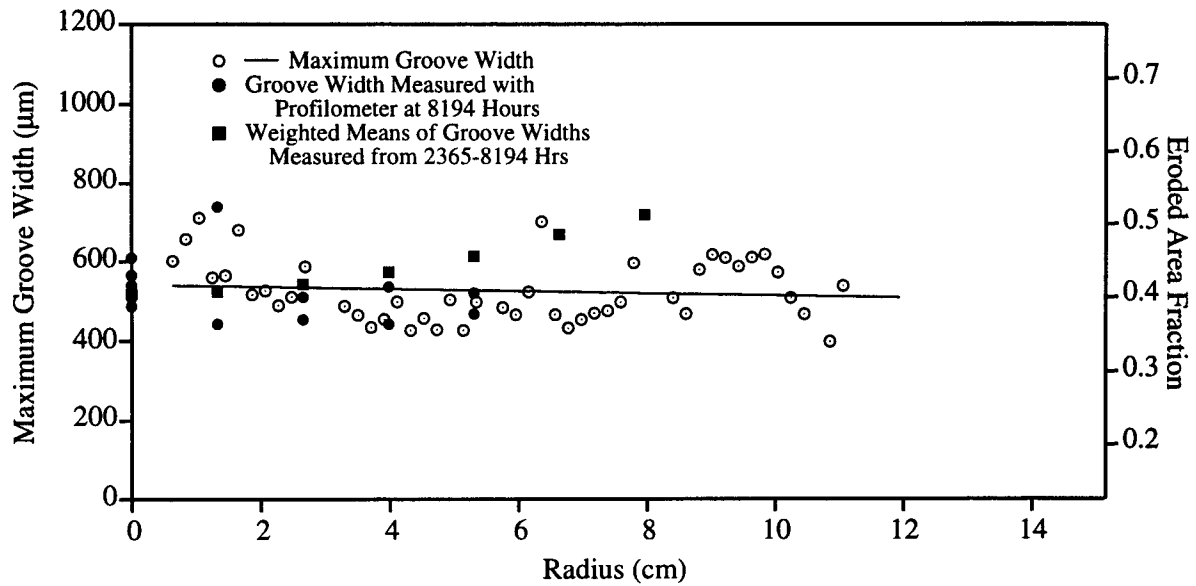


Figure 31: Variation in the width of the groove erosion on the downstream surface of the accelerator grid.

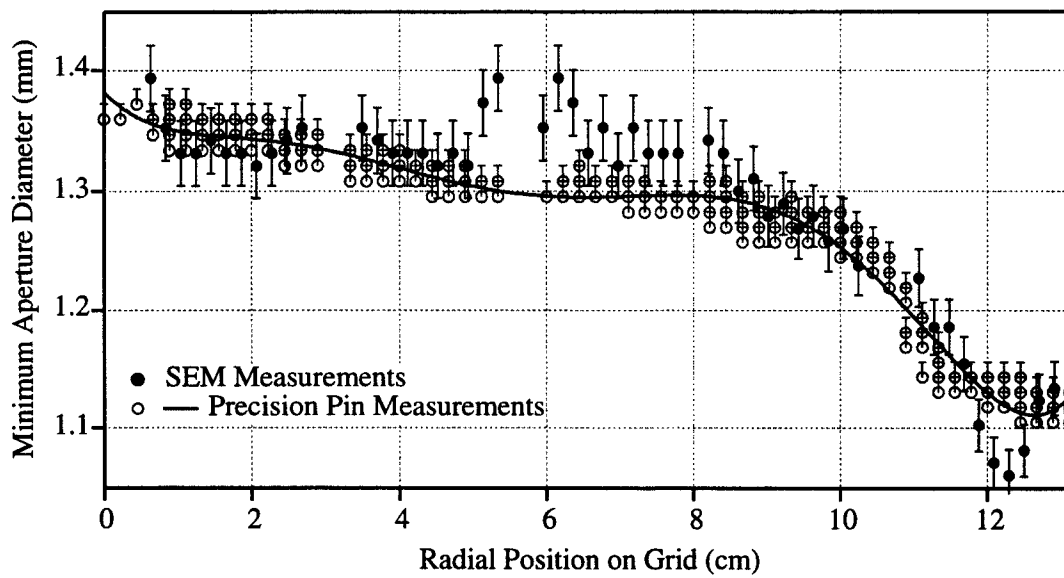


Figure 32: Post-test measurements of the accelerator grid aperture diameters.

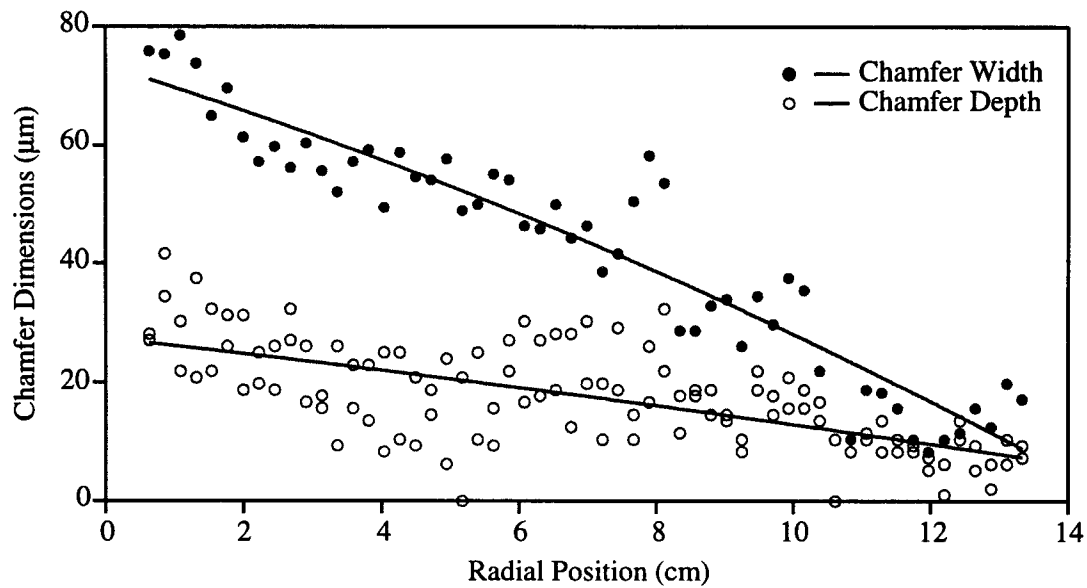


Figure 34: Chamfer dimensions measured from screen grid cross-sections.

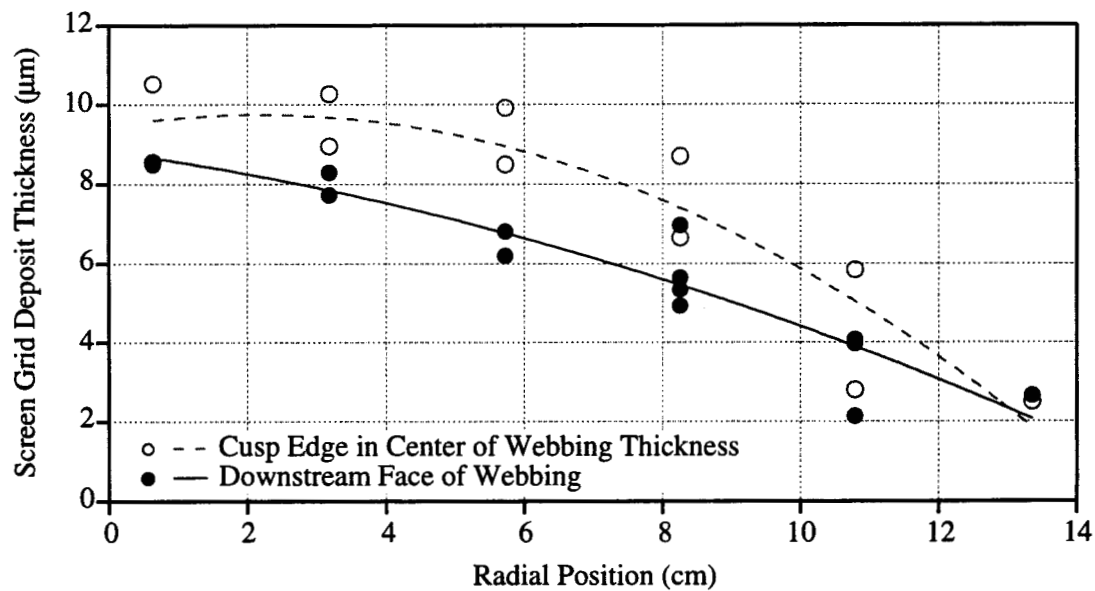


Figure 35: Thickness of molybdenum deposits on the downstream surface of the screen grid.

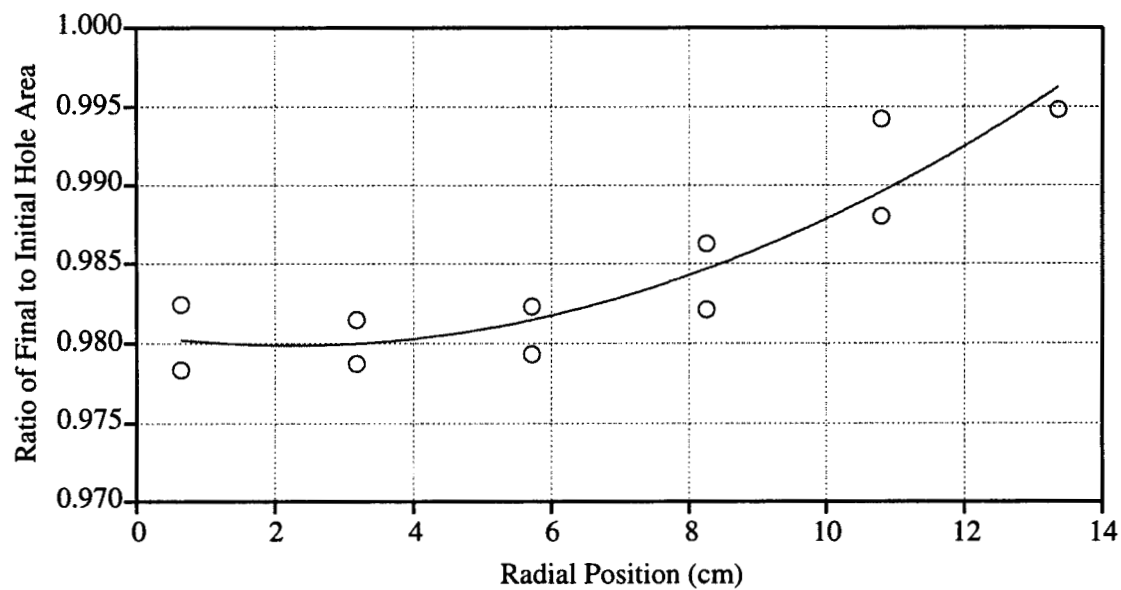


Figure 36: Effect of screen grid deposits on hole area.

Discharge Chamber

Two measures of discharge chamber performance were monitored periodically during the test—the ion production costs and the double ion production rate. These trends and post-test observations of potential life-limiting phenomena will be discussed here.

Discharge Chamber Performance. Increases in the ion production cost dominate the engine total power increase which lead to the performance degradation discussed in a previous section. The discharge losses for the various operating points are plotted in Fig. (38). The greatest increase in beam ion production cost was experienced at the lowest power level. This curve also shows the largest scatter in the measurements, a consequence of increased sensitivity to small flow rate variations [14]. The ratio of double to single ion current is shown for the nominal and throttle test points in Figures (39) and (40). The increase in double ion content could result in a slight loss in thrust at the lower power levels, but these trends are of interest primarily because of the impact on internal erosion rates. The double-to-single ion current ratio for the nominal power level was nearly constant and relatively low. At the higher throttle test points the ratio increases over the first half of the test and the values are much larger, a consequence of operating at a higher propellant efficiency.

Post-Test Inspection of the Discharge Chamber. The post-test analysis focused on characterizing the composition and size of sputter-deposited films and spalled flakes in the discharge chamber and identifying any changes in internal magnetic field strength. Very few loose flakes were found in the discharge chamber after the test. Those that were discovered varied in thickness from 2–12 μm and were composed of molybdenum, stainless steel and tantalum. Samples were laser-cut from the walls of the discharge chamber and sectioned to measure the thickness of adherent films. These were found to be only 2–5 μm thick and appeared to be very well bonded to the internal mesh and grit-blasted surfaces. These films were composed primarily of molybdenum and stainless steel. The internal magnetic field peak value was found to be the same as the initial specification, so it appears that the magnets did not degrade at the engine operating temperatures. Detailed azimuthal maps of the magnetic field did reveal an interesting

asymmetry, however. The variation in magnetic field near the downstream magnet ring shown in Fig. (41) could have resulted in an asymmetric plasma distribution and caused some of the other asymmetries noted above.

Discussion

The Life Demonstration Test has provided a wealth of information on ion engine wear processes and their effect on engine performance. Some of the important conclusions will be discussed in this section.

Wear Processes and Component Degradation

Discharge Cathode Failure Processes. The discharge cathode showed no signs of performance degradation. The wear characterization has provided a valuable clue to help identify the erosion mechanism. The data are all consistent with a source of high energy ions located just downstream of the keeper orifice. The wear sites on the keeper suggest it is subject to ion bombardment on the downstream face. It also clearly shadow-shields the cathode from this flux; the only cathode surfaces that were eroded were those exposed in the cathode keeper orifice. The surface texturing on the cathode flange suggests that it was exposed to simultaneous deposition of molybdenum and tantalum and energetic ions, but the inner region was shadowed to some extent by the keeper itself. The deposition pattern on the upstream surface of the keeper orifice plate can also be explained by bombardment from a source downstream. The sputter-deposited films contain both molybdenum and tungsten. The molybdenum from the region of net erosion on the keeper orifice wall was deposited on the cathode orifice plate and then subsequently re-sputtered onto the upstream side of the keeper orifice plate, along with tungsten from the cathode orifice plate.

The erosion on the cathode itself was minimal. The primary potential failure modes associated with the cathode assembly appear to be structural failure of the keeper orifice plate, shorts between the cathode and keeper orifice plate caused by spalling of the thick films on the upstream face of the keeper plate, and insert degradation. The keeper acts as a shield for the cathode and does erode at a lower rate than the cathode would if exposed. This is probably because the

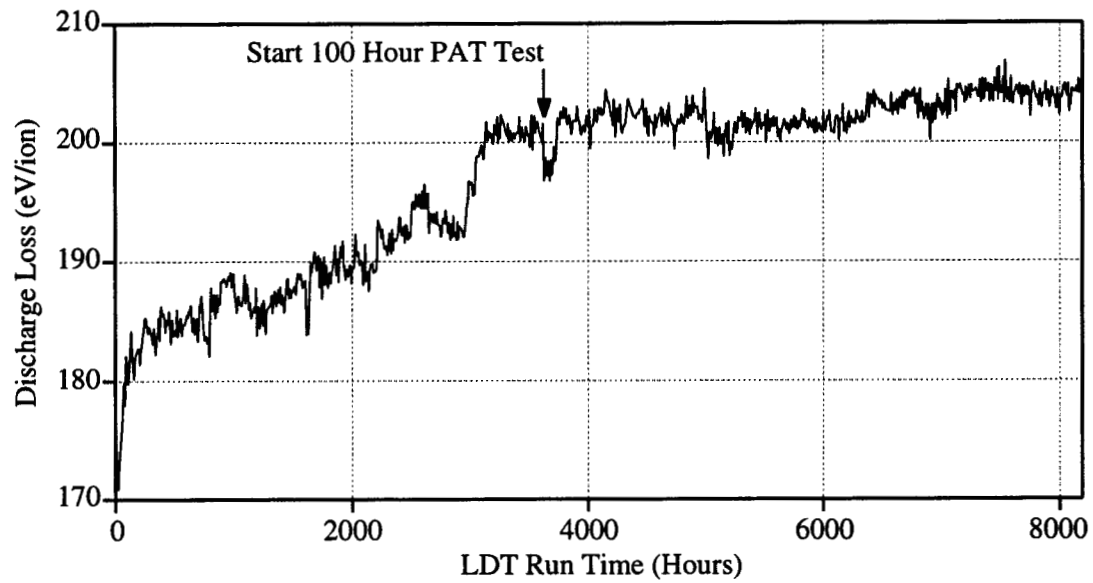


Figure 37: Variations in discharge loss at the nominal full power point.

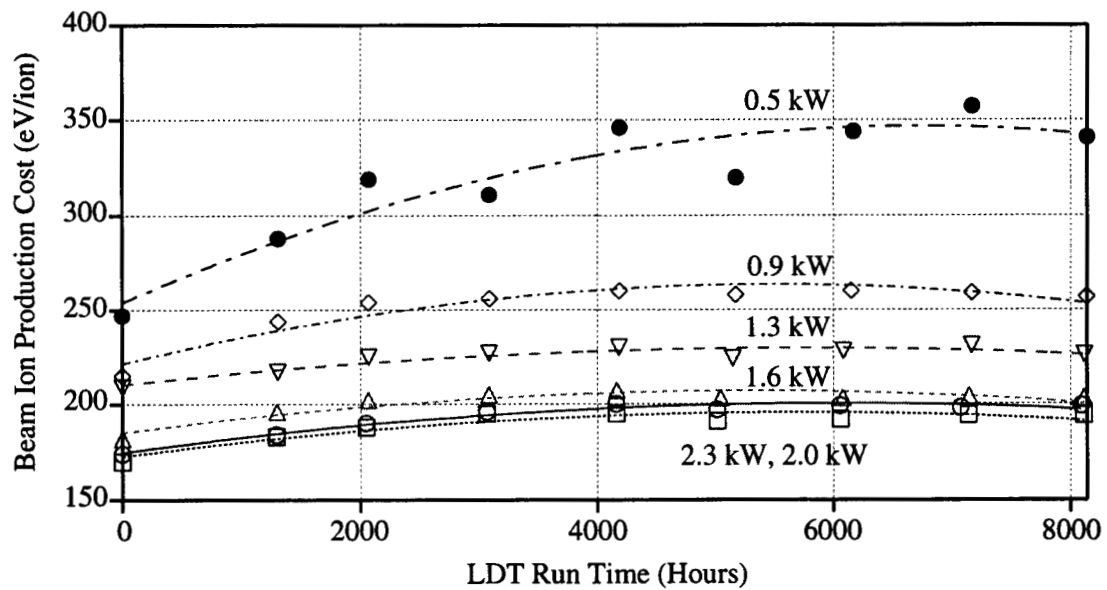


Figure 38: Variations in discharge loss at the throttle test points.

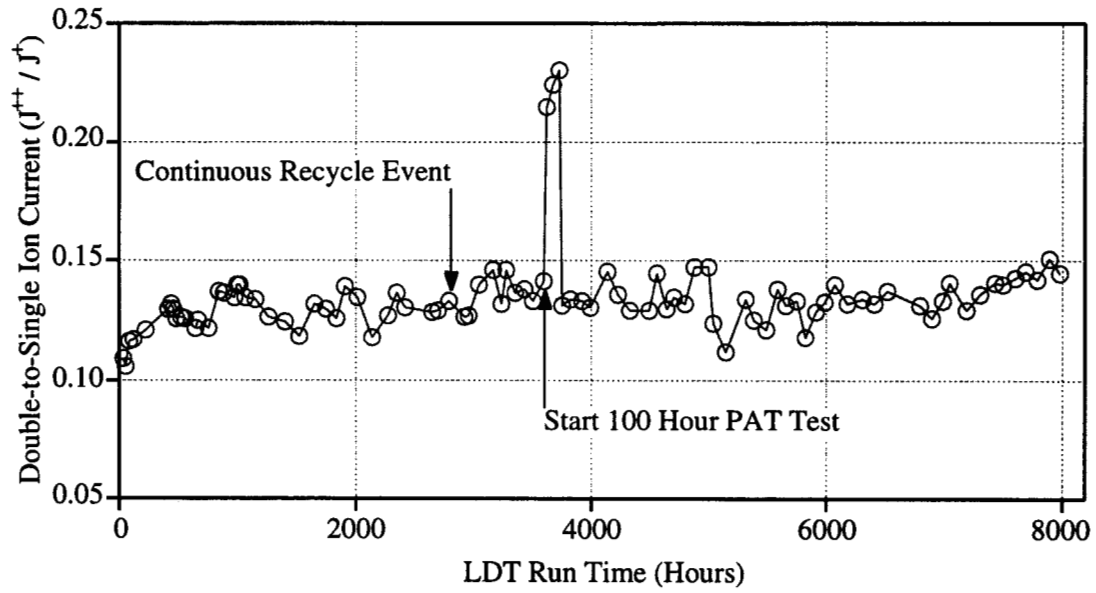


Figure 39: ExB probe measurements of the double ion content at the nominal operating point.

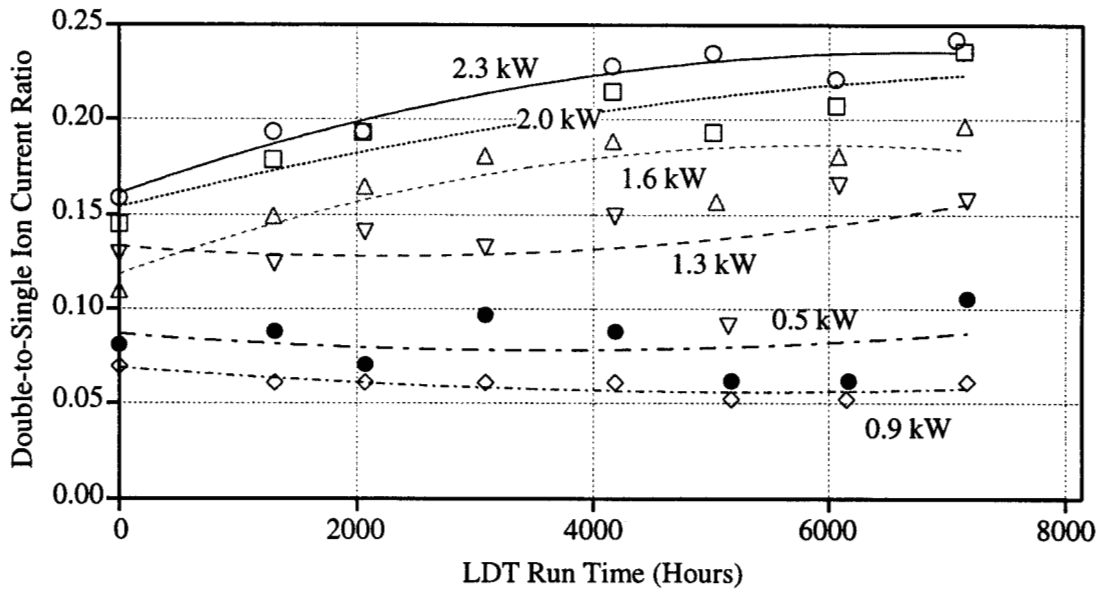


Figure 40: ExB probe measurements of the double ion content at the throttled operating points.

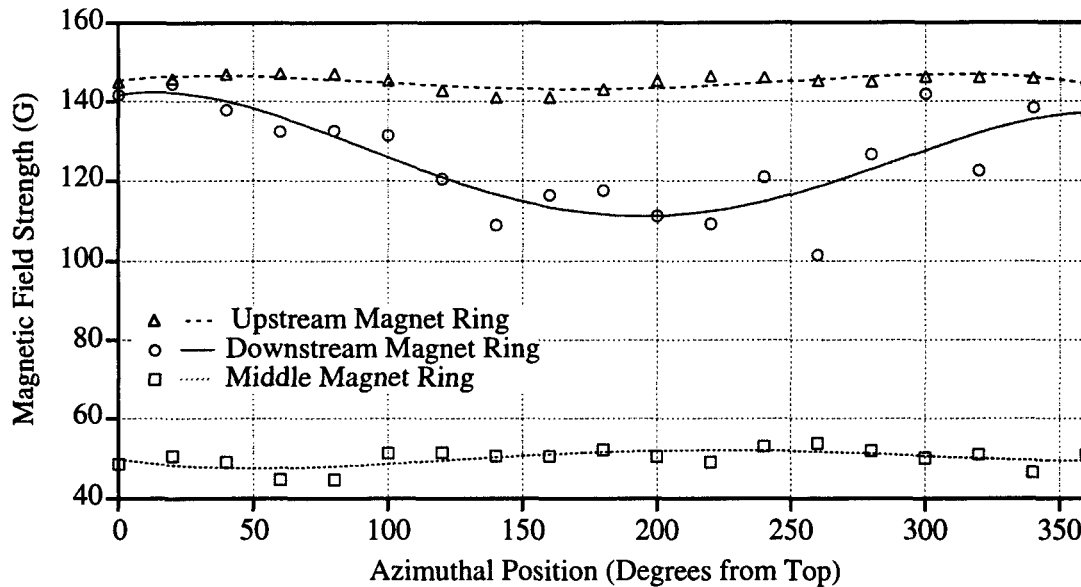


Figure 41: Asymmetries in the discharge chamber magnetic field strength.

keeper operates at about 3–5 V closer to the plasma potential, so ions strike with slightly less energy. Nevertheless, it does erode and for very long service life a thicker orifice plate may be required.

The thick films found on the upstream face of the keeper represent a previously unrecognized failure mode. They seem adherent, but the sharp corner of the orifice is a potential film failure point where flakes might start to form. Shorting between the cathode and the keeper does not necessarily cause an engine failure. It may make cathode ignition more difficult and it will increase the wear rate of the keeper by tying it to cathode potential. In subsequent designs the upstream end of the orifice should be chamfered and the interior surfaces grit-blasted to help retain the films. In addition, greater emphasis must be placed on understanding cathode erosion.

The discharge cathode insert appeared to be operating properly, but did show evidence of surface changes that could eventually lead to a failure similar to that observed by Sarver-Verhey in the 28,000 hour test of a plasma contactor cathode [17]. In that cathode tungsten deposits in the downstream end and formation of barium tungstates in the upstream por-

tion appear to have compromised the electron emission capabilities of the insert. Similar structures in the early stages of formation were found in the cathode from the LDT.

Neutralizer Cathode Failure Processes. The only real concern with the neutralizer cathode is erosion of the orifice, which is very localized. It is not clear if the erosion observed in this test is the result of a single episode or occurred gradually over time. Early changes in flight neutralizers due to a burn-in effect can't be ruled out. The observed orifice wear is probably what caused the loss of flow rate margin, and if this process leads to operation in plume mode in flight the neutralizer could be rapidly destroyed.

The neutralizer insert appeared to be in much better condition than the discharge cathode insert. There was much less evidence of the material transport processes which can ruin the emitter surface. This is probably a consequence of a lower operating temperature.

Ion Optics Failure Processes. The 1500 hour transient observed in the impingement current is most likely due to direct impingement on some portions of the optics, such as the cusps, which disappears when

the component is eroded through. The trends in perveance and electron backstreaming limits can be explained in terms of accelerator grid aperture enlargement. This results in greater perveance margin because the beamlets have more room to expand before starting to impinge directly on the hole walls. The electron backstreaming characteristics become poorer with increased aperture diameter because the hole centerline potential decreases. Analytical and numerical models of electron backstreaming have been coupled with hole wall erosion models to calculate the time dependence of the electron backstreaming limit and have achieved excellent agreement with these test data [19, 2].

The screen grid transparency changes are also indirectly related to the erosion of the accelerator grid apertures. Material removed from the accelerator grid which is deposited on the screen grid reduces the open area of the screen grid. The area change noted in Fig. (36) is quantitatively very similar to the reduction in screen grid transparency observed in the test. The chamfering of the upstream edges of the screen grid apertures may also affect the shape of the upstream sheath and reduce the effective transparency. The deposits found on the screen grid were thicker than any found in the discharge chamber, and they are forming on surfaces which have not been textured to help improve adhesion. They therefore pose the greatest risk of unclearable grid shorts. Further testing and analysis will be required to quantify and manage this risk.

A major objective of this test was to validate the assumption in some of the model used to assess the engine service life capability and provide inputs on the failure mode drivers. The assessment of failure risk associated with accelerator grid structural relies on an expression for the mass loss per unit area in the pits and grooves pattern in the grid center M_{pg}'' , which is given by

$$M_{pg}'' = \left(\frac{m_g}{e(1 - \phi_a)A_b} \right) \left(\frac{\lambda_Y \beta}{\alpha f_a} \right) J_a Y t, \quad (1)$$

where m_g is the mass of a grid atom, e is the charge of an electron, ϕ_a is the grid open area fraction, A_b is the active beam area, t is the operating time, J_a is the impingement current and Y is the sputter yield for ions at normal incidence with an energy corresponding to the sum of the grid voltage, the coupling voltage and

the beam potential relative to the ambient plasma potential. The parameter λ_Y is the ratio of the net sputter yield to Y and accounts for ions which do not fall through the entire potential in front of the grid, non-normal incidence, the presence of impurities on the grid and redeposition of sputtered material in the erosion pattern. The parameter β is the ratio of the total impingement current that is focused into the pits and grooves pattern, α represents the fraction of the webbing area covered by the erosion pattern and f_a is the mass loss flatness parameter, defined as the ratio of the average mass loss per unit area to the peak mass loss per unit area. This model essentially relates the total mass loss, which can be related to macroscopically observable parameters, to the mass lost in the pits and grooves pattern in the center of the grid, where structural failure occurs first. A failure criterion in the form of the mass loss per unit area at structural failure, which depends on the geometry of erosion, is coupled to Eq. (1) to calculate the time to failure.

A number of the assumptions behind Eq. (1) have been verified by the detailed grid erosion measurements from the LDT. In addition, critical parameters such as α are obtained from the groove widths measured in this test. The mass loss per unit area calculated from the erosion geometry characterization can be used to estimate the magnitude of some of the important life drivers. Equation (1) can be solved for the ratio $\lambda_Y \beta / f_a$ as a function of constants and parameters measured in the test. This ratio for the center hole is plotted as a function of time in Fig. (42). This demonstrates that this ratio has remained constant at about 0.22 with an uncertainty of about 0.02 throughout the test. The mass loss flatness parameter is expected to be similar to the beam current flatness parameter of about 0.46 in space, but in ground tests is generally broadened. Previous measurements on other grids have yielded values of 0.61–0.89. The parameter β represents the fraction of impingement current which is focussed into the pits and grooves. Assuming this is roughly equal to the mass loss ratio between the holes and the pits and grooves measured in this test, β is about equal to 0.5. This gives a ratio β / f_a that is of order unity, implying that the net sputter yield is only about 22 percent of the published values for normal incidence at an energy of about 200 eV. This reduction could be due to rede-

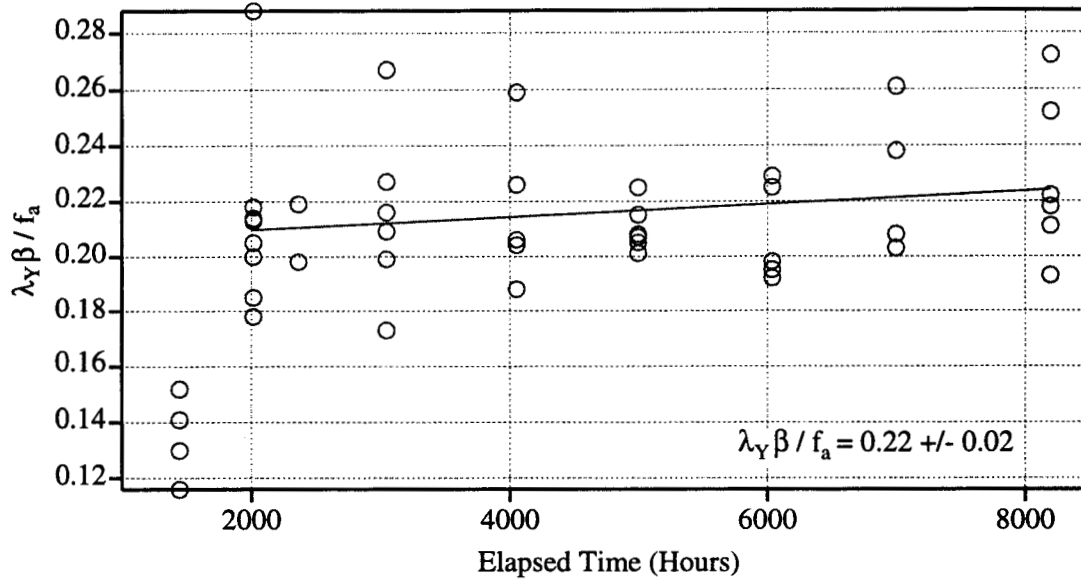


Figure 42: Variation of $\lambda_Y \beta / f_a$ during the test.

position of sputtered material in the pattern, a lower average ion energy than assumed or the effect of the deposition of carbon sputtered from the beam target onto the grid. The redeposition effect would be expected to increase in time as the erosion pattern grew deeper, but the data do not show this. There is net carbon deposition on the grid periphery and on the mesas surrounding the holes, but there is no visible evidence of carbon deposits in the pits and grooves pattern. Modeling of the surface kinetics of carbon deposited on molybdenum substrates and its effect on the molybdenum sputter yields suggests this is not an issue for the conditions of this test. At this time, it seems most likely that the average ion energy is lower than 200 eV due to significant charge exchange production in regions where the local potential is negative with respect to the beam plasma. Further modeling and testing is required to confirm this conclusion.

The loss of electron backstreaming margin is not in itself a failure mode, if additional accelerator grid voltage can be applied to compensate. However, this increases the energy of the ions striking the accelerator grid and accelerates the erosion processes. These two wear processes are therefore coupled, and the combination has been treated in [2] using data from this test.

The Effect of Wear on Performance

Shortly before the completion of the 8200 hour LDT, an analytical model of discharge chamber performance was used to identify engine wear or aging processes that could qualitatively explain the observed performance degradation [14, 20]. These processes included increased accelerator grid transparency to neutrals, decreased magnetic field strength due to magnet deterioration, variations in discharge voltage, increased discharge chamber wall temperature, increased electron temperature, increased cathode voltage, and reduced screen grid transparency to ions. New information from the post-test analysis and subsequent testing allows this list to be re-evaluated. Post-test examination of the magnetic field strength suggests no significant changes, the measured discharge voltage did not vary substantially, and there was no evidence of cathode degradation which would have increased the losses associated with electron emission. Measurements from an on-going long duration test of the DS1 flight spare engine show that the anode temperature is not changing significantly, even though the discharge losses have increased. The time history of the electron temperature is not known, but it is clear from performance data during the test and post-test analysis that the accelerator grid open area

fraction increased and the screen grid transparency decreased. It now appears that the dominant wear processes that cause engine performance degradation are in the optics. Erosion of the accelerator grid aperture walls increases the neutral loss rate, and deposition of some fraction of this material on the screen grid reduces its transparency to ions. Overall, this was an extraordinarily successful test, not only in terms of the wealth of data it returned that allowed the identification of new failure modes and the close coupling between wear and performance decay, but because the observed performance loss was so small and the wear characteristics relatively benign. This provides great confidence that these engines are capable of efficient operation for extremely long periods of time.

Acknowledgements

The authors would like to acknowledge the invaluable fabrication and test support provided by GRC's Test Installations Division as well as Al Owens, Bill Thogmartin and Bob Toomath at JPL. The support of other NSTAR Project members and technical staff including Jack Stocky, Keith Goodfellow, Mike Marcucci, Witold Sokolowski, Jim Kulleck, Ken Evans, Dave Brinza, Mike Henry, Barri Gurau, Alan Jacobson and Mike Smith (JPL) and Roger Myers (previously with NYMA, Inc.) and Frank Curran (previously of GRC) is also gratefully acknowledged. The research described in this paper was conducted at the Jet Propulsion Laboratory, California Institute of Technology, and was sponsored by the National Aeronautics and Space Administration.

References

- [1] J.E. Polk, R.Y. Kakuda, J.R. Anderson, J.R. Brophy, V.K. Rawlin, M.J. Patterson, J.S. Sovey, and J. Hamley. Validation of the NSTAR Ion Propulsion System on the Deep Space One Mission: Overview and Initial Results. In *35th Joint Propulsion Conference*, Los Angeles, CA, 1999. AIAA-99-2274.
- [2] J.R. Brophy, C.E. Garner, J.E. Polk, and J. Weiss. The Ion Propulsion System on NASA's Space Technology 4/Champlion Comet Rendezvous Mission. In *35th Joint Propulsion Conference*, Los Angeles, CA, 1999. AIAA-99-2856.
- [3] M.J. Patterson and T. Haag. Performance of the 30-cm Lightweight Ion Thruster. In *23rd International Electric Propulsion Conference*, Seattle, WA, 1993. AIAA-93-108.
- [4] J. S. Sovey et al. Development of an Ion Thruster and Power Processor for New Millenium's Deep Space 1 Mission. In *33rd Joint Propulsion Conference*, Seattle, WA, 1997. AIAA-97-2778.
- [5] J.R. Brophy, C.E. Garner, J.E. Polk and K.D. Goodfellow. Methods for Cryopumping Xenon. In *32th Joint Propulsion Conference*, Lake Buena Vista, FL, 1996. AIAA-96-3206.
- [6] J.E. Polk et al. A 1000-Hour Wear Test of the NASA NSTAR Ion Thruster. In *32nd Joint Propulsion Conference*, Lake Buena Vista, FL, 1996. AIAA-96-2717.
- [7] J. A. Hamley et al. Development Status of the NSTAR Ion Propulsion System Power Processor. In *31st Joint Propulsion Conference*, San Diego, CA, 1995. AIAA-95-3305.
- [8] T. W. Haag. Design of a Thrust Stand for High Power Electric Propulsion Devices. In *25th Joint Propulsion Conference*, Monterey, CA, 1989. AIAA-89-2829.
- [9] J.E. Polk, J.R. Anderson and J.R. Brophy. Behavior of the Thrust Vector in the NSTAR Ion Thruster. In *34rd Joint Propulsion Conference*, Cleveland, OH, 1998. AIAA-98-3940.
- [10] J.R. Anderson and D. Fitzgerald. Experimental Investigation of Fullerene Propellant for Ion Propulsion. In *23rd International Electric Propulsion Conference*, Seattle, WA, 1993. AIAA-93-033.
- [11] J.E. Polk, J.R. Anderson, J.R. Brophy, V.K. Rawlin, M.J. Patterson, and J. Sovey. In Situ, Time-Resolved Accelerator Grid Erosion Measurements in the NSTAR 8000 Hour Ion Engine Wear Test. In *25th International Electric Propulsion Conference*, Cleveland, OH, 1997. IEPC 97-047.

- [12] J.R. Brophy, J.E. Polk, and V.K. Rawlin. Ion Engine Service Life Validation by Analysis and Testing. In *32nd Joint Propulsion Conference*, Lake Buena Vista, FL, 1996. AIAA-96-2715.
- [13] M. Patterson, T. Haag, V. Rawlin, and M Kussmaul. NASA 30 cm Ion Thruster Development Status. In *30th Joint Propulsion Conference*, Indianapolis, 1994. AIAA-94-2849.
- [14] J.E. Polk, J.R. Anderson, J.R. Brophy, V.K. Rawlin, M.J. Patterson, and J.S. Sovey. The Effect of Engine Wear on Performance in the NSTAR 8000 Hour Ion Engine Endurance Test. In *33rd Joint Propulsion Conference*, Seattle, WA, 1997. AIAA-97-3387.
- [15] V.K. Rawlin. NSTAR Memorandum: Screen Grid Wear at Low Flow and High Beam Current Conditions. Technical report, Lewis Research Center, Cleveland, OH, 1996.
- [16] M.J. Patterson, V.K. Rawlin, and J.S. Sovey. 2.3 kW Ion Thruster Wear Test. In *31st Joint Propulsion Conference*, San Diego, CA, 1995. AIAA-95-2516.
- [17] T.R. Sarver-Verhey. Destructive Evaluation of a Xenon Hollow Cathode After a 28,000 Hour Life Test. In *34rd Joint Propulsion Conference*, Cleveland, OH, 1998. AIAA-98-3482.
- [18] J.E. Polk, J.R. Brophy, and J.Wang. Spatial and Temporal Distribution of Ion Engine Accelerator Grid Erosion. In *31st Joint Propulsion Conference*, San Diego, CA, 1995. AIAA-95-2924.
- [19] J.R. Anderson, K.D. Goodfellow, J.E. Polk, and R.F. Shotwell. The Results of an 8200 Hour Wear Test of the NSTAR Ion Thruster. In *35th Joint Propulsion Conference*, Los Angeles, CA, 1999. AIAA-99-2857.
- [20] J.R. Brophy. Ion Thruster Performance Model. Technical Report NASA CR-174810, Colorado State University, Fort Collins, CO 80523, 1984.